Materials Chemistry and Physics 252 (2020) 123279

Contents lists available at ScienceDirect

Materials Chemistry and Physics

journal homepage: www.elsevier.com/locate/matchemphys

Polarization dependent infrared reflectivity studies of Si-doped MOCVD grown GaN/Sapphire epilayers

Devki N. Talwar [a,b,*], Hao-Hsiung Lin [c], Zhe Chuan Feng [d,e,**]

[a] Department of Physics, University of North Florida, 1 UNF Drive, Jacksonville, FL, 32224-7699, USA
[b] Department of Physics, Indiana University of Pennsylvania, 975 Oakland Avenue, 56 Weyandt Hall, Indiana, PA, 15705-1087, USA
[c] Graduate Institute of Electronics Engineering and Department of Electrical Engineering, National Taiwan University, Taipei, 10617, Taiwan
[d] Laboratory of Optoelectronic Materials & Detection Technology, Guangxi Key Laboratory for the Relativistic Astrophysics, School of Physical Science & Technology, Guangxi University, Nanning, 530004, China
[e] State Key Laboratory of Luminescence and Applications, Changchun Institute of Optics, Fine Mechanics and Physics, Chinese Academy of Sciences, Changchun, 130033, China

HIGHLIGHTS

- Polarization dependent reflectivity is used to comprehend structural and phonon traits of Si-doped GaN/Sapphire epifilms.
- A 4 × 4 transfer matrix method is adopted with surface and interface roughness to explain the infrared spectroscopy data.
- Simulated reflectivity results validated surface morphology noticed in TEM and AFM.
- Angular dependent infrared transmission is crucial to assess the charge carrier density, N.

GRAPHICAL ABSTRACT

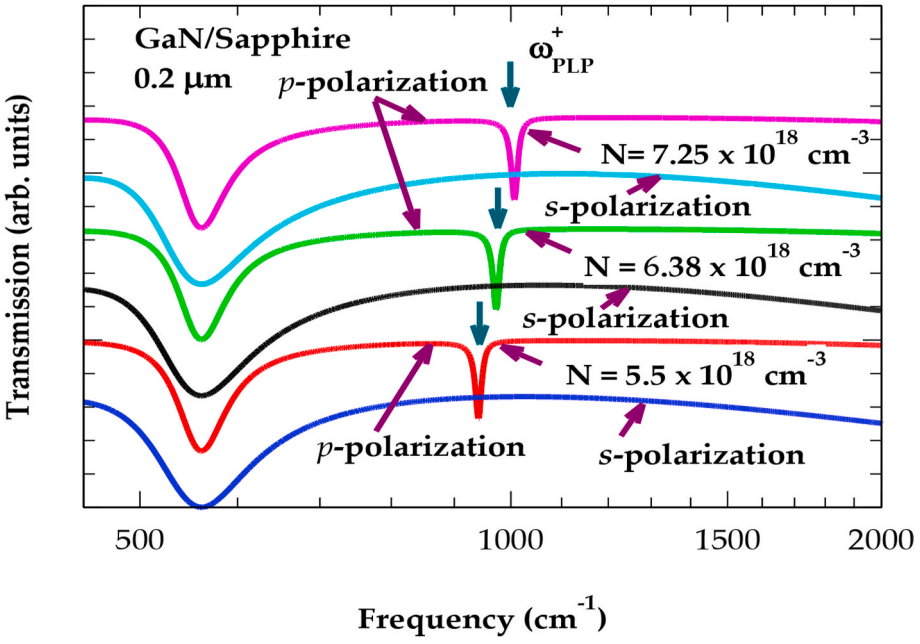

* Corresponding author. Department of Physics, University of North Florida, 1 UNF Drive, Jacksonville, FL, 32224-7699, USA.
** Corresponding author. Laboratory of optoelectronic materials & detection technology, Guangxi Key Laboratory for the Relativistic Astrophysics, School of Physical Science & Technology, Guangxi University, Nanning, 530004, China.
E-mail addresses: d.talwar@unf.edu (D.N. Talwar), fengzc@gxu.edu.cn (Z.C. Feng).

https://doi.org/10.1016/j.matchemphys.2020.123279
Received 19 February 2020; Received in revised form 14 May 2020; Accepted 25 May 2020
Available online 20 June 2020

ARTICLE INFO

Keywords:
Polarization dependent infrared reflectivity
MOCVD method
Surface and interface roughness
Si-doped GaN/Sapphire epifilms
Transmission electron and atomic force microscopy

ABSTRACT

Comprehensive experimental and theoretical studies are reported on the infrared reflectance (IRR)/transmittance (IRT) spectra to empathize the vibrational and structural properties of Si-doped GaN films grown on sapphire substrate using metal-organic chemical vapor deposition technique. Systematic analysis of the IRR/IRT spectra is achieved in the framework of a 4 × 4 transfer matrix methodology by meticulously including both the surface roughness and effective transition layer. With careful simulations, we have demonstrated that it is possible to achieve a very good fit to the polarization dependent reflectivity spectra of Si-doped GaN/Sapphire – allowing to ascertain film thickness *d*, charge carrier concentration N, root-mean squared roughness and many other parameters. In the context of Berreman effect, our investigations of IRT spectra for an ultrathin Si-doped GaN film in the oblique geometry has provided a direct evidence of identifying the optical phonons and coupled plasmon-longitudinal-optical phonon modes, in good agreement with the IRR and Raman scattering spectroscopy (RSS) data. From these results, we strongly believe that the measurements of IRT spectra in obliquely incident radiation should be considered as a complementary tool to the RSS for epitomizing doped III-Ns and/or any other ultrathin films of technologically important compound semiconductor materials.

1. Introduction

Group III-Ns (AlN, GaN and InN) have gained considerable attention in recent years due to their potential demands for conceiving various electronic and optoelectronic devices [1–20]. Synthesizing ternary alloys ($A_xB_{1-x}N$, with A, B =Al, Ga and In) have provided greater flexibility of tuning energy band gaps $E_g(x)$ from near infrared (N-IR) to deep ultraviolet (D-UV) region. The benefits of using III-Ns over many other wide bandgap semiconductors are related to their exceptional electrical, structural and mechanical properties viz., low dielectric constant; large break down field; high thermal conductivity; higher bond strength; high temperature/radiation resistance, etc. These traits have made them valuable for designing not only short-wavelength laser diodes, blue-green light-emitting diodes (LEDs), sensors, detectors, photocatalysts, high-temperature, high-power, high-frequency, high-density data storage devices for energy application [7,8] but also exploiting them in space-exploration [14] needs.

Among other III-Ns, GaN is the most promising material. It crystallizes in 2H- wurtzite (wz); 3C- zinc blende (zb); and rock-salt (rs) structures. Usually, the GaN is grown on a sapphire (Al_2O_3) c-plane substrate (c-axis perpendicular to the sample surface) has the hexagonal wz structure. Major issues that hindered the early progress of using GaN in device applications included (*a*) the growth and reproducibility of crystalline morphology [21,22], (*b*) pervasive unintentional n-type conductivity [23–26], (*c*) lack of efficient p-type dopants [27–30], and (*d*) the absence of lattice matched/thermally compatible substrates [31–36]. Controlled growth of GaN/Sapphire films has been achieved [21,22] by using a metal-organic chemical vapor deposition (MOCVD) with a two-step process. The films, however, exhibited high density of various defects especially in the interface region, and often with a rough surface [37–39].

Reactivation of Mg acceptors (a^-) to attain p-type doping [27–30] in GaN with adequate free hole concentration helped fabricate p-n junction blue LEDs. Despite these successes there are many challenges for improving the quality of n- and/or p-doped GaN/Sapphire epifilms [21–36]. For commercial use of III-Ns, it is equally essential to identify both the intrinsic and/or doped impurities – assess their influence on structural, electrical and optical properties. While the Si dopant in III-V compound semiconductors acts as an amphoteric defect [40,41] – its role in GaN is either sparse and/or contradictory [42–44]. While several reports exist on the electrical properties of Si-doped GaN [1–18,42–44] – a few studies are known [37–39], however, on the structural properties of Si-doped GaN/Sapphire films.

Infrared reflectance (IRR)/transmittance (IRT) [45–53] and Raman scattering spectroscopy (RSS) [54–59] are considered highly apposite for identifying phonon traits of both perfect and/or imperfect semiconductors. Many researchers preferred, however, using IRR over the RSS as the former technique is one of the fast-turnaround methods for establishing key optical parameters of semiconductor materials. Earlier, we have exploited the IRR spectroscopy [49] at near normal incidence and successfully characterized zb 3C–SiC films grown on (001) Si by chemical vapor deposition method. A two-component Bruggeman model was adopted to elucidate atypical divots observed within the reststrahlen band region [48,49] by assuming the coexistence of crystalline and intergranular grains – forming the heterogeneous 3C–SiC films. In GaN/Sapphire samples, there are reports [37–39,51–53] which relate the observed diminishing average reflectance of interference fringe contrasts at higher frequencies, to the surface roughness. Yet, the methods used in those papers to examine the reflectance spectra remained limited to being qualitative.

Plasmon-LO-phonon (PLP) coupling is one of the most important phenomena observed [50–56] in doped semiconductors. It is normally perceived by RSS [54–56] for appraising the charge carrier concentration N. The optical detection of PLP modes by IRR has also been possible [50–53]. Such investigations by IRR spectroscopy are carried out for both the low doped n-GaN [51] ($N < 2 \times 10^{17}$ cm^{-3}) and high Si-doped [50,52] GaN/Sapphire epitaxial layers (3.1×10^{17} cm$^{-3} \leq N \leq 3.6 \times 10^{19}$ cm^{-3}). However, theoretical analysis of IRR response reported in Refs. [50–53] have considered assuming GaN layers to be isotropic despite the wz structure and the fact that Berreman [60] resonance is observed at the A_1 (LO) mode frequency. As E_1 (LO) and A_1 (LO) phonons belong to different crystal directions, proper assignment of these modes requires anisotropic data treatment [61–63].

In this paper, we have reported a comprehensive experimental and theoretical study of IRR/IRT spectra on several Si-doped GaN/Sapphire films prepared using MOCVD technique (cf. Sec. 2). A classical 4 × 4 transfer matrix method [62] is adopted to calculate the frequency dependent dielectric functions by considering both the orientation and geometry of the samples (cf. Sec 3). The effects of surface roughness and effective transition layer (ETL), detected (cf. Sec. 2.1.1-2.1.3) in the transmission electron microscopy (TEM) and atomic force microscopy (AFM) are meticulously included in the formalism (cf. Sec. 4). Evidence is offered for the influence of surface roughness and ETL on the observed IRR spectra of Si-doped GaN/Sapphire epifilms. With these factors, it is demonstrated that a very good fit to the polarization dependent reflectivity spectra of Si-doped GaN/Sapphire samples is possible – allowing one to accurately determine film thickness *d*, charge carrier concentration N, root-mean squared roughness and many other parameters influencing the IRR spectra. In the context of Berreman effect [60], our simulation of the IRT spectra for an ultrathin Si-doped GaN film in the oblique geometry has provided a direct evidence of identifying optical phonons and coupled plasmon-LO-phonon modes – in very good

Table 1
Basic properties of the MOCVD grown undoped (#S_0) and Si-doped GaN/Sapphire (#S_1 – #S_5) samples. The values of charge carrier concentration N ($10^{17}cm^{-3}$), film thickness d (μm) and mobility μ (cm^2/V s) are extracted appropriately from the Hall, IRR and RSS measurements (see: text).

Sample	N ($10^{17}cm^{-3}$) Fitted Hall [b] IRR [a] Raman [b]	d (μm) Fitted XRD [b] IRR [a]	μ (cm^2/V s) Fitted Hall [b] IRR [a] Raman [b]
S_0 (undoped)	0.327	3.58 3.61	
S_1	3.58 3.36 3.72	2.43 2.47	295 295 383
S_2	6.57 9.07 8.83	1.94 1.95	227 225 272
S_3	4.85 5.10 5.20	1.99 2.00	268 265 330
S_4	7.65 11.2 9.95	2.03 2.05	209 207 243
S_5	2.77 2.87 3.08	1.62 1.67	374 384 410

[a] This work.
[b] Ref. [57,58].

agreement with the IRR [50–52] and visible RSS [54–56] measurements. From these results, we strongly believe that IRT spectral measurements in obliquely incident radiation should be considered as a complementary tool to RSS for characterizing doped III-Ns or any other ultrathin compound semiconductor materials (cf. Secs. 4 and 5) of technological importance.

2. Experimental details

2.1. Growth and characterization of n-GaN/sapphire

A two-step MOCVD growth process [21,22] was employed to prepare high-quality Si-doped GaN samples with film thickness ranging between 1 and 4 μm on (0001) oriented sapphire substrate. An ultrathin (~25 nm) buffer layer was added first on sapphire at low temperature (450 °C) followed by depositing GaN films at high temperature (1050 °C). The role of buffer layer was to help form thermodynamically stable wz structure during post-buffer GaN growth. For the epitaxial growth of GaN – trimethylgallium (TMG) and ammonia (NH_3, 100%) were utilized as the primary chemical precursors. Mono-silane (SiH_4) was used for transforming GaN into n-type. Several Si-doped GaN epifilms (#S_1–S_5) were prepared under the same growth conditions with SiH_4 flux systematically modulated to achieve different doping levels. All n-GaN/-Sapphire samples were characterized [57,58] by RSS, secondary ion mass spectroscopy (SIMS), x-ray diffraction (XRD), AFM and TEM methods to estimate film thickness d and the surface roughness. Free charge carrier concentration N and mobility μ were derived from Hall, sheet resistivity and IRR measurements. The mobility from Hall (IRR) study was found decreasing from 374 (384) cm^2/V s for N around ~ 2.77 (2.87) x 10^{17} cm^{-3} to 209 (207) cm^2/V s for N ~ 7.65 (11.2) x10^{17} cm^{-3}.

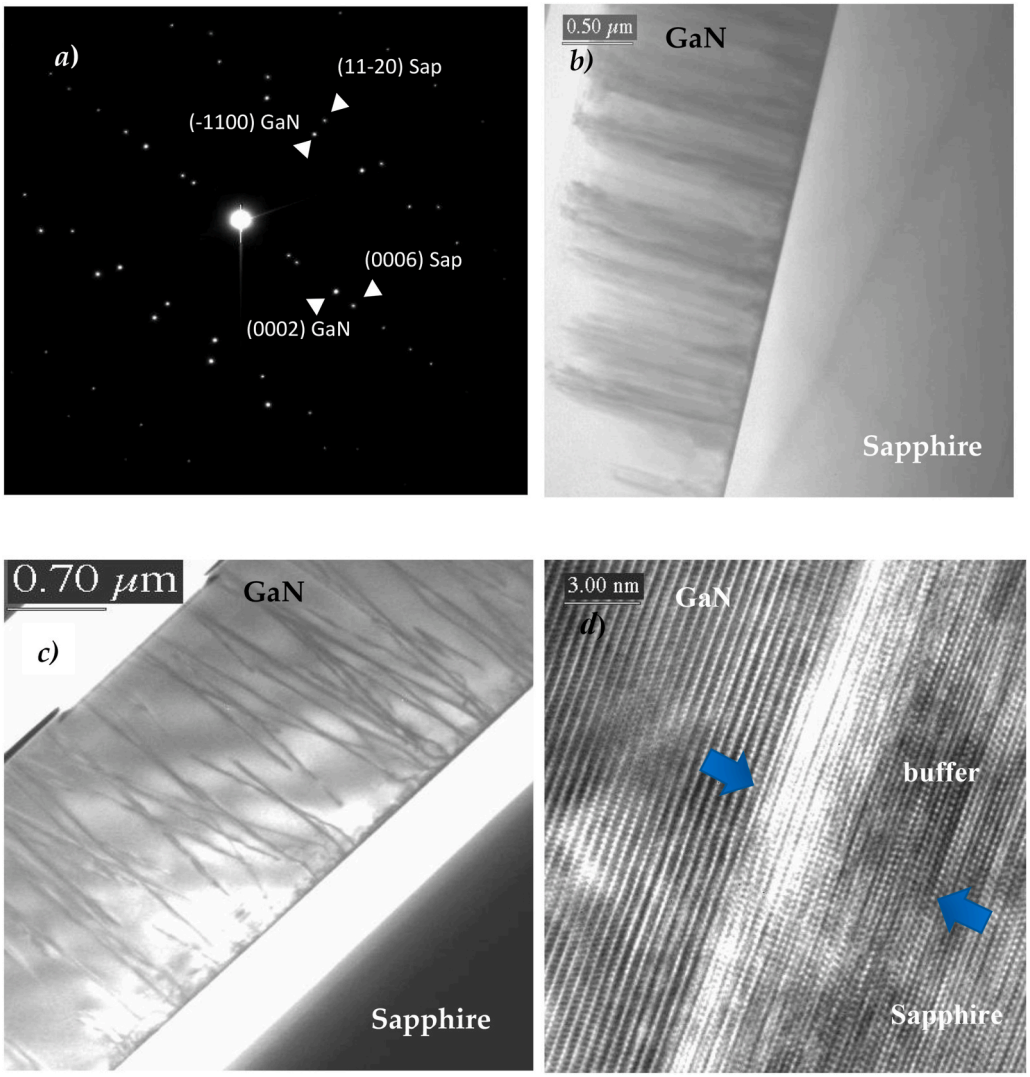

Fig. 1. (a) Electron diffraction pattern of GaN/Sapphire interface. Cross-section (XTEM) images of two MOCVD grown samples: Undoped #S_0 (b), and Si-doped GaN #S_4 (c). High resolution TEM image (d) of GaN/Sapphire interface #S_0 (see: text).

The estimated μ and N amounts to $\geq$90% of the total Si-concentration suggested a very low compensation ratio. A very good quality of the undoped GaN/Sapphire (sample #S_o) of d ~3.6 μm was also prepared exhibiting n-type behavior with N ~3.27×10^{16} cm^{-3} (cf. Table 1) due to the presence of residual oxygen (O) donors.

2.2. Electron diffraction

Electron diffraction patterns from an MOCVD grown GaN/Sapphire sample exhibit six-fold symmetry characteristics of a hexagonal monoclinic material – confirmed by diffraction from the cross-section sample and high-resolution electron micrograph (see: Fig. 1 a)). The $(\bar{1}100)$ planes of GaN layers are seen parallel [35,36] to the $(11\bar{2}0)$ Al_2O_3 planes (i.e., $[0001]_{Al2O3}||$ $[0001]_{GaN}$) with a measured lattice mismatch of around ~ 16%.

2.2.1. Cross-sectional TEM

The bright field cross-sectional TEM (XTEM) image shown in Fig. 1 b) is for an undoped GaN (#S_0) sample and Fig. 1 c) is for Si-doped GaN (#S_4) sample. Both images show dislocation lines from the interface to GaN film surface with high threading dislocation densities: the threading dislocation density in undoped GaN is about ~ 9×10^8 cm^2, while in Si-doped GaN it is about ~ 6×10^8 cm^2.

In Fig. 1 d) the high resolution TEM (HRTEM) image of an undoped GaN/Al_2O_3 interface is displayed. The sapphire region is shown in the right-lower corner while the GaN film region is in the left upper area – the middle area between the two arrow symbols is the transition buffer layer region where the obvious strain contrasts are visible.

2.3. Atomic-force microscopy

The 3D-AFM images displayed in Fig. 2 a) and Fig. 2 b) reveal surface morphologies on an undoped (#S_0) sample and Si-doped GaN/Sapphire (#S_4) sample, respectively. Clearly the surface thickness fluctuation in undoped sample (20.51 nm) is nearly ~1.6 times larger than that of the Si-doped sample (12.67 nm). This observation has corroborated our TEM results and supported a general perception that Si tends to condense the region surrounding dislocations, thus modifying the GaN surface [57,58].

2.4. Infrared spectroscopy

By using a nitrogen purged PerkinElmer 2000 spectrometer with resolution of ~2 cm^{-1}, we recorded room temperature (RT) IRR spectra on six MOCVD grown GaN/Sapphire samples (#S_0–S_5) over the wavenumber (wavelength) range of 250 cm^{-1} to 6500 cm^{-1} (40 μm–1.54 μm). The spectral studies near the normal incidence were carried out by using a mercury cadmium telluride (MCT) detector and KBr beamsplitter. Deuterated triglycine sulphate (DTGS) detector and 6-μm-thick Mylar beam-splitter were used for collecting data in the range of 250 cm^{-1} to 1000 cm^{-1}. To obtain polarized light in the far-infrared and mid-infrared regions, we used polyethylene and wire grid KRS-5 polarizer, respectively. Aluminum and gold mirrors were employed as their absolute reflectance provided references for spectral measurements in

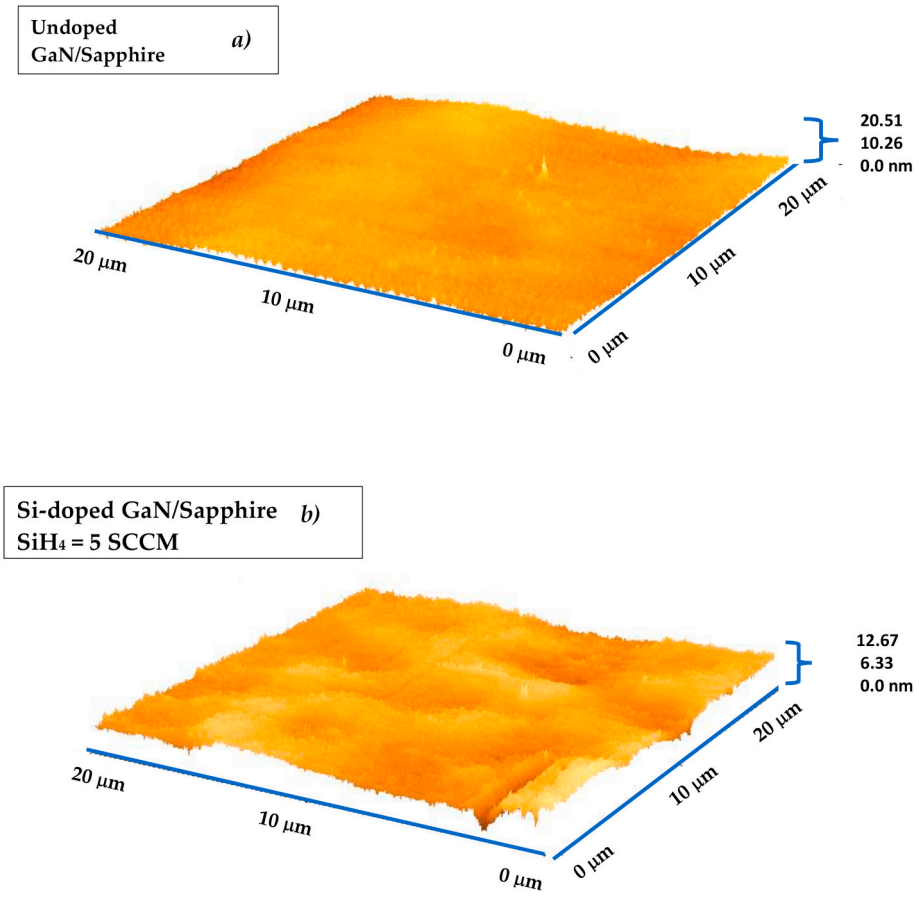

Fig. 2. AFM images of two MOCVD grown samples: (a) Undoped #S_0 and (b) Si-doped #S_4 (see: text).

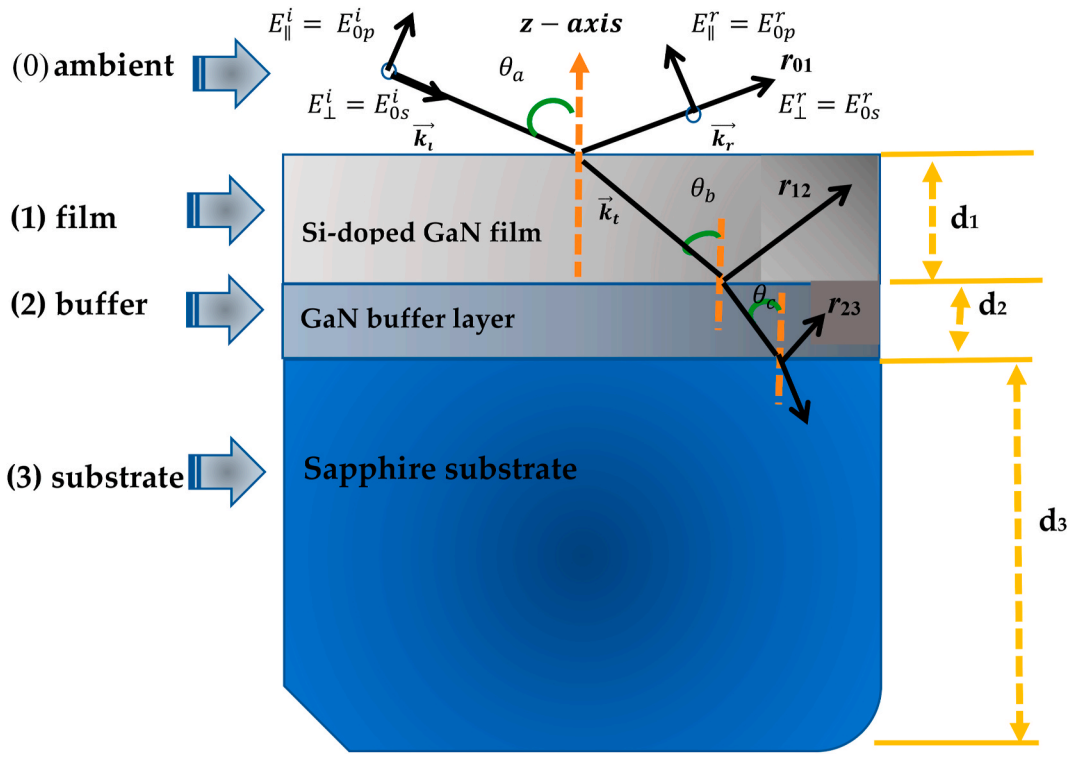

Fig. 3. Sketch of an ideal model used for simulating the infrared reflectivity (transmission) spectra for Si-doped GaN thin film (thickness d_1) with a thin GaN buffer-layer (thickness d_2) grown on a thick sapphire substrate by using a two-step metal-organic chemical vapor deposition (MOCVD) technique. The direction of incident (reflected) far-infrared radiation with *s* and *p* polarized electric field ($E_{\perp}^{i(r)} = E_{0s}^{i(r)}$ and $E_{\|}^{i(r)} = E_{0p}^{i(r)}$) components of wave vector $\overrightarrow{k_{i(r)}}$ at an oblique angle θ_a to the surface of thin film (see text).

the two respective regions. All the MOCVD grown samples were carefully examined taking multiple scans to ensure repeatability of reflectivity with interference fringes above the reststrahlen band regions. To systematically analyze the IRR spectra, we summarized the salient features of the optical response theory in Secs. 3.1–3.2. The effects of (cf. Secs. 4.1–4.2) film thickness *d*, phonon damping γ (plasma damping, γ_P), charge carrier concentration N (plasma frequency, ω_P), transition layer and surface/interface roughness are meticulously included. The simulated results of IRR spectra are compared/contrasted with the experimental data (cf. Sec. 4) and concluding remarks presented in Sec. 5.

3. Theoretical background

3.1. Optical response theory

For the anisotropic n-GaN epilayers with a thin GaN buffer layer grown on sapphire by a two-step MOCVD method, we have simulated the optical response to the infrared radiation by using a classical 4 × 4 transfer matrix method [62]. A 3-layer structure (see: Fig. 3) is employed showing the plane electromagnetic wave incident at an angle θ_a with reflectivity contributions to interference merging from ambient to the substrate. This methodology can be extended to calculate the reflectivity and/or transmission spectra of a multi-layer system with arbitrary number of films of varied thickness.

For brevity, we have reiterated here the essential mathematical formulation following Schubert et al. [62] where the complete structure is classified with numbers "0" (for ambient), "1" (for film 1), …, and "n+1" (for the substrate) having layer thickness d_1, d_2, …, and d_{n+1}, respectively. The dielectric functions of ambient, film layers and substrate material are indicated by $\tilde{\varepsilon}_0$, $\tilde{\varepsilon}_1$, …,and $\tilde{\varepsilon}_{n+1}$, respectively. In order to effectively describe the optical response to the media structure, it is necessary to have the complete dielectric tensor $\tilde{\varepsilon}(\omega)$ available in the *x*-*y* plane (perpendicular to the c-axis, $\tilde{\varepsilon}(\omega)_{\perp} = \tilde{\varepsilon}_x = \tilde{\varepsilon}_y$) as well as in the *z*-plane (parallel to the c-axis, $\tilde{\varepsilon}(\omega)_{\|} = \tilde{\varepsilon}_z$):

$$\tilde{\varepsilon}(\omega) = \begin{bmatrix} \tilde{\varepsilon}(\omega)_{\perp} & 0 & 0 \\ 0 & \tilde{\varepsilon}(\omega)_{\perp} & 0 \\ 0 & 0 & \tilde{\varepsilon}(\omega)_{\|} \end{bmatrix} = \begin{bmatrix} \tilde{\varepsilon}_x & 0 & 0 \\ 0 & \tilde{\varepsilon}_y & 0 \\ 0 & 0 & \tilde{\varepsilon}_z \end{bmatrix}, \quad (1)$$

In this approach, the total transfer matrix $\widehat{M}_T[= \widehat{M}_{in}\widehat{M}_1\widehat{M}_2\widehat{M}_{ex}]$ can be written as a product: $\widehat{M}_{in}\widehat{M}_1\widehat{M}_2\widehat{M}_{ex}$ – where the terms $\widehat{M}_{in}$, $\widehat{M}_{ex}$ represent the incident and exit matrices, respectively. The $\widehat{M}_1$ and $\widehat{M}_2$ are related to the propagation matrix $\widehat{M}\ (d)^{-1}$ which include the effects of crystal's anisotropic properties and phase shifts induced by the layer thickness of n-GaN as well as the underlying GaN template. The matrix $\widehat{M}_{in}$ which depends only on the incident angle θ_a and the index of refraction $\hat{n}_a$ of the ambient, can be written as [62]:

$$\widehat{M}_{in} = \begin{bmatrix} 0 & 1 & -(1/\hat{n}_a)\cos\theta_a & 0(1/\hat{n}_a)\cos\theta_a & 0 \\ 0 & 1 & 0 & (1/\hat{n}_a) & \\ (1/\cos\theta_a) & 0 & 0 & (1/\hat{n}_a) & \\ -(1/\cos\theta_a) & 0 & & & \end{bmatrix} \quad (2)$$

The general form of matrix $\widehat{M}$ is expressed as:

$$\widehat{M} = \begin{bmatrix} \cos(k_i d\,\widehat{N}_{xz}) & 0 & 0 & i\left(\frac{\widehat{N}_{xz}}{\tilde{\varepsilon}_x}\right)\sin(k_i d\,\widehat{N}_{xz}) \\ 0 & \cos\left(k_i d\,\widehat{N}_{yy}\right) & -i\left(\frac{1}{\widehat{N}_{yy}}\right)\sin\left(k_i d\,\widehat{N}_{yy}\right) & 0 \\ 0 & -i\left(\widehat{N}_{yy}\right)\sin\left(k_i d\,\widehat{N}_{yy}\right) & \cos\left(k_i d\,\widehat{N}_{yy}\right) & 0 \\ -i\left(\frac{\tilde{\varepsilon}_x}{\widehat{N}_{xz}}\right)\sin(k_i d\,\widehat{N}_{xz}) & 0 & 0 & \cos(k_i d\,\widehat{N}_{xz}) \end{bmatrix}, \tag{3}$$

Table 2
The optical phonon parameters of c- Sapphire (Al_2O_3) (*a*) and GaN (*b*) used in the two-layer model for calculating the dielectric functions and reflectivity spectra (see: text).

(a) Sapphire.

	ε_∞	ω_{TO} (cm^{-1})	S	γ_{TO} (cm^{-1})
E_u	$\varepsilon_{\infty\perp} = 3.077$	385.0	0.22	7.00
		439.1	2.88	3.05
		569.0	3.04	5.56
		633.6	0.20	7.17
A_{2u}	$\varepsilon_{\infty\parallel} = 3.072$	398.0	6.73	3.49
		582.4	1.68	1.58

(b) GaN.

ε_∞	ω_{TO} (cm^{-1})	ω_{LO} (cm^{-1})	$\gamma = \gamma_{TO}$ (cm^{-1}) = γ_{LO}(cm^{-1})
$\varepsilon_{\infty\parallel} = 5.31$	533 A_{1TO}	735 A_{1LO}	5.0
$\varepsilon_{\infty\perp} = 5.35$	561 E_{1TO}	743 E_{1LO}	5.0

where d is the film thickness; $k_i (= 2\pi/\lambda)$ is the incident wavevector with wavelength λ. The terms $\widehat{N}_{xz}$ and $\widehat{N}_{yy}$ can be obtained [62] by applying Snell's law using incident angle θ_a.

$$\widehat{N}_{xz} = \sqrt{\tilde{\varepsilon}_x}\sqrt{1 - \left[\left(\frac{1}{\sqrt{\tilde{\varepsilon}_z}}\right)sin\theta_a\right]^2}, \tag{4}$$

$$\widehat{N}_{yy} = \sqrt{\tilde{\varepsilon}_y}\sqrt{1 - \left[\left(\frac{1}{\sqrt{\tilde{\varepsilon}_y}}\right)sin\theta_a\right]^2}. \tag{5}$$

The exit matrix $\widehat{M}_{ex}$ has the form:

$$\widehat{M}_{ex} = \begin{bmatrix} 0 & 0 & \cos\theta_z & 0 \\ 1 & 0 & 0 & 0 \\ -\sqrt{\tilde{\varepsilon}_{sy}}\cos\theta_y & 0 & 0 & 0 \\ 0 & 0 & \sqrt{\tilde{\varepsilon}_{sx}} & 0 \end{bmatrix}, \tag{6}$$

$$R_s = \left|\frac{M_{10}M_{22} - M_{12}M_{20}}{M_{00}M_{22} - M_{02}M_{20}}\right|^2, \tag{7}$$

$$R_p = \left|\frac{M_{30}M_{02} - M_{32}M_{00}}{M_{20}M_{02} - M_{22}M_{00}}\right|^2. \tag{8}$$

It is to be noted that in the *s*-polarized mode having electric field vector ***E*** perpendicular to the optic axis, the R_s spectra contains information about the ordinary dielectric function – exhibiting comparable spectral shapes under different angles of incidence except the intensities (cf. Secs. 4.1–4.2). In the *p*-polarized case, however, the electric field vector ***E*** is parallel to the plane of incidence instigating the reflectivity R_p of the extraordinary mode. This means that, the *p*-polarized reflectance (R_p) is sensitive to the angles of incidence (cf. Sec. 4.1) and it exhibits unique spectral response with anisotropic optical properties.

3.2. Dielectric function of anisotropic materials

In polar semiconductors, the complex dielectric function $\tilde{\varepsilon}(\omega)$ can be expressed as a linear superposition of susceptibilities with contributions emanating from bound valence electrons (bve), lattice vibrations (lat), free charge carriers (fcc) and impurities (imp), etc. – provided there are no interactions of these processes with each other [62]:

$$\tilde{\varepsilon}(\omega) = 1 + \chi_{bve} + \chi_{lat} + \chi_{fcc} + \chi_{imp} + \ldots, \tag{9}$$

In the infrared region, the impact of χ_{bve} to the dielectric function is frequency independent. Therefore, in Eq. (9) one can replace the term $(1 + \chi_{bve})$ by a high frequency dielectric constant, ε_∞. To evaluate the contribution of lattice vibrations χ_{lat} and free carrier concentration χ_{fcc} – we have adopted the classical Lorentz and Drude oscillator models [49, 62,63]. The influence of χ_{imp} on $\tilde{\varepsilon}(\omega)$ is considered as a part of the lattice vibrations. For anisotropic materials the perpendicular $\{\tilde{\varepsilon}(\omega)_\perp\}$ and parallel $\{\tilde{\varepsilon}(\omega)_\parallel\}$ components of the dielectric function to the crystal c-axis can be evaluated by using [62]:

$$\tilde{\varepsilon}(\omega)_{\perp(\parallel)} = \varepsilon_{\infty\perp(\parallel)}\left[1 - \frac{\omega^2_{p\perp(\parallel)}}{\omega\left(\omega + i\,\gamma_{p\perp(\parallel)}\right)}\right] + \varepsilon_{\infty\perp(\parallel)}\sum_j\left[\frac{\omega^2_{j,LO\perp(\parallel)} - \omega^2_{j,TO\perp(\parallel)}}{\left(\omega^2_{jTO\perp(\parallel)} - \omega^2 - i\,\gamma_{\perp(\parallel}\,\omega\right)}\right], \tag{10a}$$

$$= \varepsilon_{\infty\perp(\parallel)}\left[1 - \frac{\omega^2_{p\perp(\parallel)}}{\omega\left(\omega + i\,\gamma_{p\perp(\parallel)}\right)}\right] + \sum_j\frac{S_{j,\perp(\parallel)}\omega^2_{j,TO\perp(\parallel)}}{\left(\omega^2_{j,TO\perp(\parallel)} - \omega^2 - i\,\gamma_{j,\perp(\parallel}\,\omega\right)}, \tag{10b}$$

where $\tilde{\varepsilon}_{sx}$ and $\tilde{\varepsilon}_{sy}$ are the anisotropic dielectric functions of the sapphire substrate. The angles θ_y and θ_z can also be obtained from the Snell's law. Once the total transfer matrix is computed using Eq. (3), the *s*- and *p*-polarized reflectance can be readily obtained [62]:

where, the characteristic plasma frequency $\omega_{p\|(\perp)} = \sqrt{\frac{4\pi N_{\|(\perp)}\,e^2}{m^*_{e\perp(\parallel)}\varepsilon_{\infty\perp(\parallel)}}}$ de-

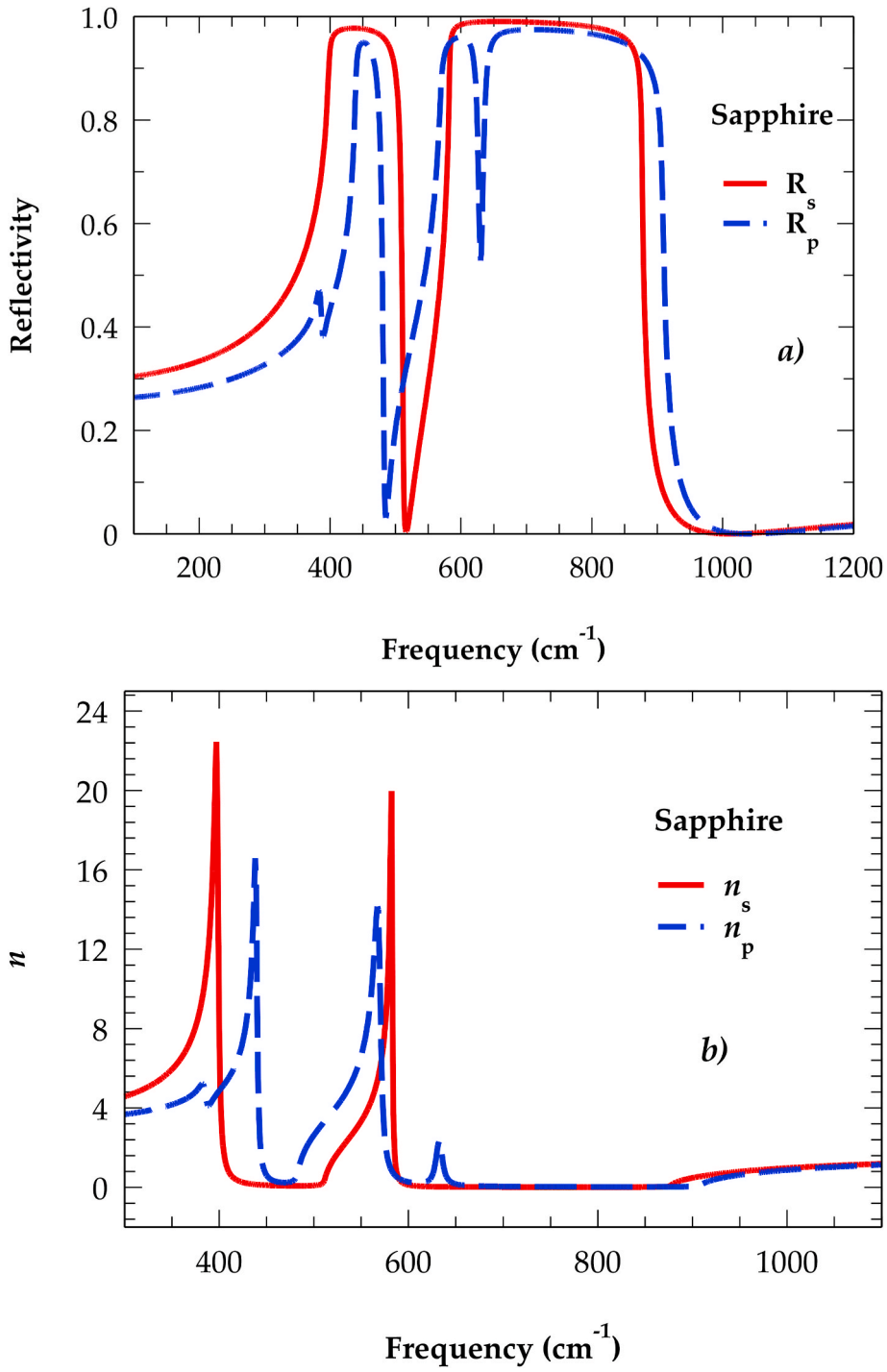

Fig. 4. Simulated results of (a) infrared reflectivity [R_s (red line), R_p (blue dotted line)], (b) refractive index [n_s (red line), n_p (blue dotted line)], (c) extinction coefficient [k_s (red line), k_p (blue dotted line)], and (d) comparison of experimental (blue open circles) and calculated (redline) reflectivity spectra of c-sapphire (see: text). (For interpretation of the references to color in this figure legend, the reader is referred to the Web version of this article.)

pends upon the free carrier concentration $N_{||(\perp)}$ and effective electron mass m_e^*. The parameters $\gamma_{p\perp(||)}$ $(\gamma_{\perp(||)})$ signify the plasma (phonon) damping constants; the term $\omega_{TO||(\perp)}$ $(\omega_{LO||(\perp)})$ denotes the polar-optical phonon frequency $\omega_{A1TO(E1TO)}$ $\omega_{A1LO(E1LO)})$ and $S_{j,\perp(||)}$ implies its oscillator strength. The mobility $\mu_{||(\perp)}$ of free carriers can be determined by using$\mu_{||(\perp)} = \frac{e}{m^*_{e||(\perp)}\gamma_{||(\perp)}}$. One must note that we have treated here the effective mass, mobility and charge carrier concentration, isotropically.

3.3. Dielectric function of the substrate

In order to assess the accuracy of simulated IRR/IRT spectra against the experimental data for undoped and Si-doped GaN/Sapphire films – it is necessary to have the optical phonon frequencies and dielectric function known for the substrate. For sapphire (α-Al_2O_3), Schubert et al. [62] have reported the spectroscopic ellipsometry results on the dielectric function and anisotropy of phonon modes near $\vec{q} = 0$. As α-Al_2O_3, exhibits a rhombohedral structure comprising of hexagonal

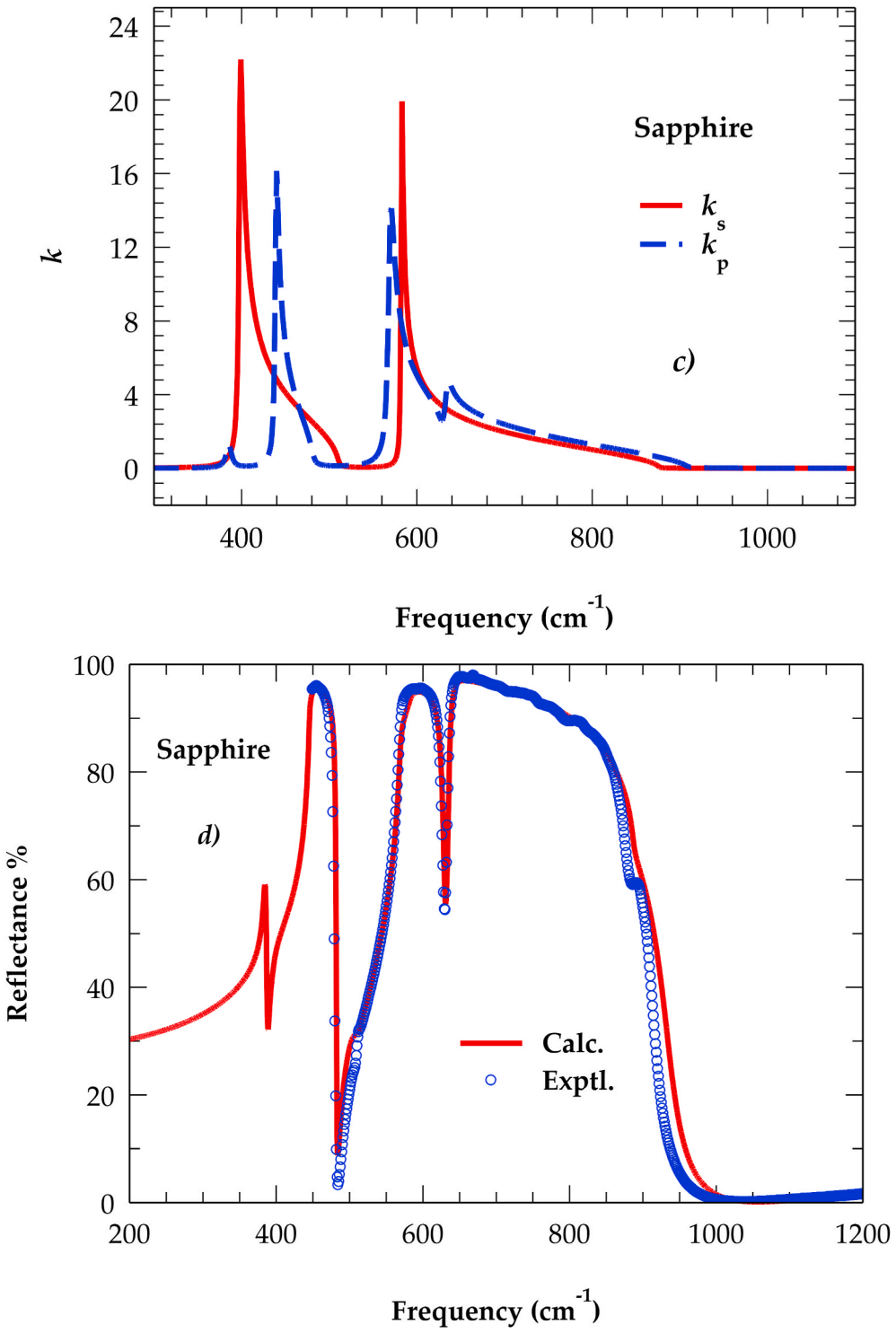

Fig. 4. (*continued*).

close packed (hcp) lattice with Al and O atoms at the octahedral sites – the group theoretic analysis of the irreducible representation for the D^6_{3d} point group symmetry indicated optical phonons near $\vec{q} = 0$ in the form [62]:

$$\Gamma^{opt}_{D^6_{3d}} = 2A_{1g} + 2A_{1u} + 3A_{2u} + 2A_{2u} + 5E_g + 4E_u, \quad (11)$$

where the two A_{1g} and five E_g modes are Raman active – the two A_{2u} and four E_u type modes are infrared (IR) active while the remaining two A_{1u} and three A_{2g} modes are neither Raman nor IR active.

By employing a classical two-layer (ambient/sapphire) model one can calculate (cf. Sec. 4) the dielectric function $\tilde{\varepsilon}(\omega)$ [or $\tilde{n}(\omega)$ ($\cong \sqrt{\tilde{\varepsilon}(\omega)}$)] of α-Al_2O_3. Both real ε_1 and imaginary ε_2 parts of $\tilde{\varepsilon}(\omega)$ are required for appraising $n(\omega)$, $k(\omega)$ of $\tilde{n}(\omega)$:

$$\tilde{n}(\omega) = n(\omega) + i\,k(\omega) = \sqrt{\tilde{\varepsilon}(\omega)}\,, \quad (12)$$

where

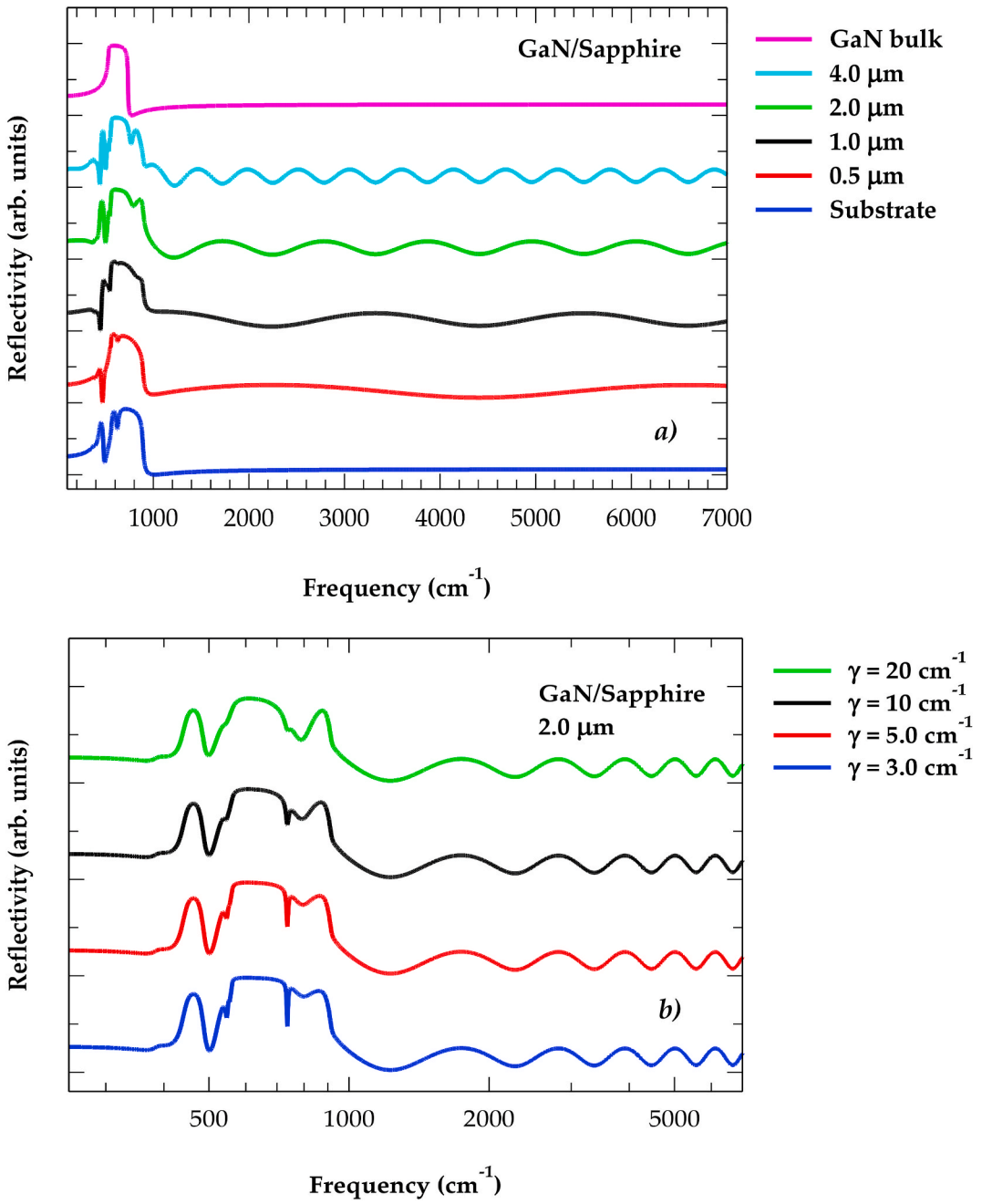

Fig. 5. Simulated reflectivity spectra displaying the effects of: (a) film thickness in GaN/Sapphire epifilms, (b) phonon damping constant γ, (c) plasma frequency ω_P with a fixed plasmon damping constant γ_P (= 100 cm^{-1}), and (d) plasmon damping constant γ_P with a fixed plasma frequency ω_P (= 600 cm^{-1}) on a 2 μm thick n-GaN film (see: text).

$$n(\omega) = \left[\frac{\left(\varepsilon_1^2 + \varepsilon_2^2\right)^{\frac{1}{2}} + \varepsilon_1}{2}\right]^{\frac{1}{2}}, \tag{13a}$$

and

$$k(\omega) = \left[\frac{\left(\varepsilon_1^2 + \varepsilon_2^2\right)^{\frac{1}{2}} - \varepsilon_1}{2}\right]^{\frac{1}{2}}, \tag{13b}$$

are, respectively the refractive index, and extinction coefficient.

4. Results and discussion

Comprehensive simulation of the IRR and IRT spectra for n-GaN/Sapphire films is complicated due to the needs of incorporating several factors, viz., (*a*) the effects of film thickness, (*b*) phonon γ (plasma γ_P) damping, carrier concentration N or ω_P, (*c*) coupling between *s*- and *p*-polarized light at the medium interface, and (*d*) surface roughness as well as ETL at the GaN/air and GaN/Sapphire interfaces, respectively. If one sets the c-axis of sapphire perpendicular to the GaN epifilm – it results in no cross conversion of *s*- and *p*-polarized light. The simulations of IRR and IRT for the undoped GaN/Sapphire sample can be further simplified by neglecting ETL, surface and/or interface roughness.

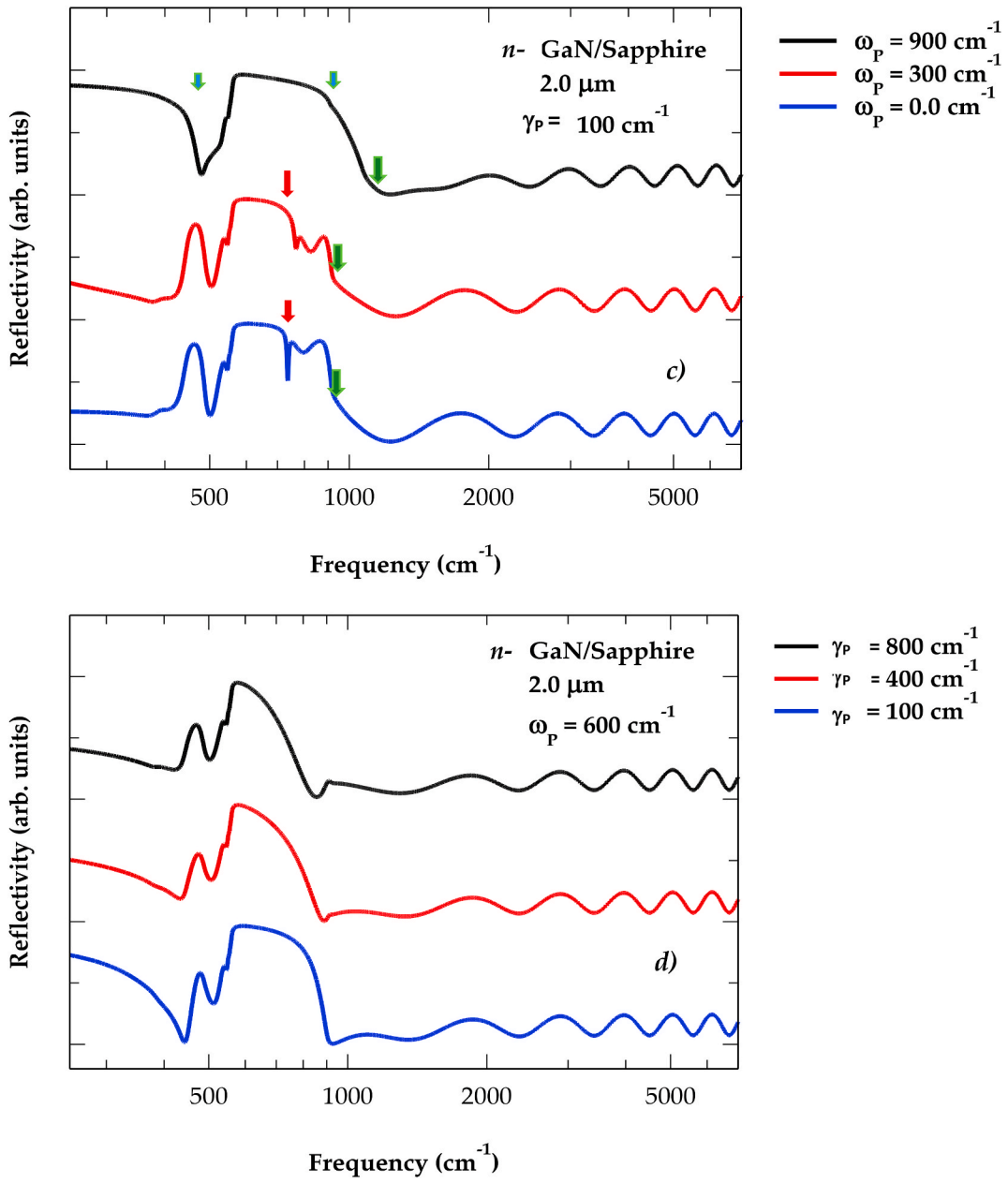

Fig. 5. (*continued*).

4.1. Infrared spectra

Before integrating different aspects as outlined above in the modified optical response theory (cf. Secs. 3.1–3.3), we first used an ideal prototype and calculated the IRR and IRT spectra of uniaxial GaN/Sapphire by adopting a three-phase model with parameter values from Table 2 a-b) – treating the substrate as a thick semi-infinite material. Two-phase (ambient/sapphire) scheme is exploited for simulating the dielectric function $\tilde{\varepsilon}(\omega)$ [or$\tilde{n}(\omega)$ ($\cong \sqrt{\tilde{\varepsilon}(\omega)}$)] of α-Al_2O_3. The results (see: Fig. 4 a-c)) of$R_{s(p)}(\omega)$, $n_{s(p)}(\omega)$ and $k_{s(p)}(\omega)$ along with the total reflectivity of sapphire shown in Fig. 4 d) have revealed a very good agreement with the experimental data [62]. The influence of various parameters on the IRR and IRT are discussed next.

4.1.1. Ideal GaN/Sapphire

Calculated reflectivity spectra (R) of the perfect GaN/Sapphire with different film thickness d, is displayed in Fig. 5 a) along with the results of substrate and bulk GaN. The perusal of Fig. 5 a) revealed some interesting results of R in three spectral regions (*i*) $\omega < \omega_{A1(TO)}$, (*ii*) $\omega_{E1(TO)} < \omega < \omega_{A1(LO)}$, and (*iii*) $\omega > \omega_{E1(LO)}$. For bulk GaN, the maximum value (~95%) of R is emerged at ω_{TO} due to resonance between incident photons and lattice vibrations. It has exhibited a minimum near 750 cm^{-1} (just above ω_{LO}) and attained constant value of ~20% at frequency $\omega > 800$ cm^{-1}. With the increase of film thickness, the reflectivity also showed well developed bulk-like GaN features with interference fringes appearing on both sides of the reststrahlen band. In an earlier study Tiwald et al. [63], have affirmed that the reflectance R of a thick epilayer can become comparable to that of the bulk material as phonon damping limits the penetration depth of infrared light.

One must note that for GaN/Sapphire, the contrasts in the interference fringes of IRR spectra at $\omega \gg \omega_{E1(LO)}$ occurs due to differences in the refractive indices [62,63] of epifilm (n_f) and substrate (n_s) while the film thickness d instigates variation in the fringe spacing ($\Delta\omega$). Moreover, our study revealed that the vibrational features of sapphire substrate overlapping with the reststrahlen band of GaN makes it difficult

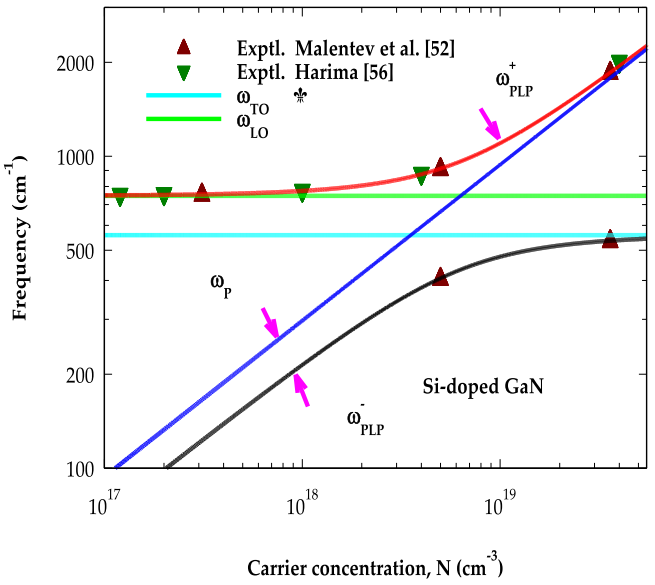

Fig. 6. The charge carrier-density N dependence plasmon-LO-phonon modes ($\omega^{\pm}_{PLP}$) for Si-doped GaN. The ω_{LO} and, ω_{TO} phonons are represented by green color line and sky blue color line, respectively; the high frequency ω^{+}_{PLP}, low frequency ω^{-}_{PLP} and plasma ω_P mode frequency are shown by red, black and blue color lines, respectively. The experimental bottle green colored inverted triangles represent the experimental Raman scattering results of Harima Ref. [56], and cherry brown colored triangles are the infrared reflectivity results of Melentev et al. Ref. [52]. (see text). (For interpretation of the references to color in this figure legend, the reader is referred to the Web version of this article.)

Table 3
Heavily doped n-GaN samples #M1 and #M2 grown epitaxially by Melentev et al. [Ref. [52]] of different thickness *d* (μm) and charge carrier concentration N ($10 \times {}^{18}$ cm^{-3}) used in the infrared reflectivity measurements. Based on our theoretical simulations we provided values (in wavenumbers (cm^{-1})) for the plasma frequency ω_P, high and low frequency ω^{+}_{PLP}, ω^{-}_{PLP} PLP modes (see: text).

Sample #	*d* [a)] (μm)	N [a)] ($10 \times {}^{18}$ cm^{-3})	ω_P [b)] (cm^{-1})	ω^{+}_{PLP} [b)] (cm^{-1})	ω^{-}_{PLP} [b)] (cm^{-1})
M1	10	5.00	664	913	406
M2	6.2	36.0	1782	1857	536

[a] Ref. [52].
[b] This work.

identifying the phonon traits of GaN/Sapphire films. We need an effective optical response theory to compare the simulated IRR and IRT results of GaN/Sapphire with experimental data. To appraise the observed damping behavior in the Fabry-Perot fringes at $\omega > 800$ cm^{-1} we have meticulously included surface roughness and ETL in the classical theory [62]. The impacts of ETL and surface roughness are carefully assessed by examining (cf. Sec. 4.1.5) the simulated IRR spectra with the experimental data.

4.2. Effects of phonon and plasma damping

To understand the effects of phonon (plasma) γ (γ_P) damping and ω_P on the IRR spectra – we have displayed in Fig. 5 b) – d) the simulated results of a 2 μm thick GaN/Sapphire. In undoped film ($\omega_P = 0$) as the phonon damping is increased (cf. Fig. 5 b)) we find a dip near A_1 (LO) mode decreasing and even disappearing for larger γ. For fixed value of γ_P as free carrier concentration N (or ω_P) is increased – our simulations revealed (cf. Fig. 5 c)) significant changes in the reflectivity spectra especially in the restsrahlen band region – identifying three prominent features: (*i*) a dip near A_1 (LO) becoming weaker and gradually fading (see: red color arrows), (*ii*) the interference phonons below E_1 (TO) and above A_1 (LO) become frailer and ultimately vanish (see: light blue color arrows), and (*iii*) a minimum flat position above the E_1 (LO) mode shifts to higher frequency (see: green color arrows). The later feature is believed to be allusive to the PLP coupling. In Fig. 5 d) the influence of mobility μ (γ_P) on reflectivity of n-GaN/Sapphire epifilm is displayed for a fixed value of ω_P. One may also note that the decrease of μ (or increase of γ_P) not only lowers the reflectivity below the reststrahlen band but also reduces its bandwidth.

4.2.1. Estimating N in Si-doped GaN/Sapphire

In doped semiconductors, the LO phonons strongly interact with the free carrier plasmons through electric fields to produce two PLP ($\omega^{\pm}_{PLP}$) modes. The traits of $\omega^{\pm}_{PLP}$ modes are highly dependent on the plasmon frequency ω_P. If ω_P is lower than the frequency of ω_{LO} phonon, then ω^{-}_{PLP} behaves as a plasmon-like and ω^{+}_{PLP} acts as a phonon-like. The frequency of ω^{+}_{PLP} mode increases with N and its character changes from phonon-like to plasmon-like at higher N [62].

In heavily doped GaN, the $\omega^{\pm}_{PLP}$ modes are observed by IRR [50–52] and RSS [54–56] spectroscopy to assess the charge carrier concentration. In Fig. 6, we have plotted the variations of $\omega^{\pm}_{PLP}$ modes as a function of N. In Si-doped GaN/Sapphire epifilms (see: Table 1) – the sample #S_4 has the largest carrier density N ≈ 1.12 × 10^{18} cm^{-3}. In these (#S_1-#S_5) films, the calculated values of ω_P ($\leq\approx$ 314 cm^{-1}) and ω^{-}_{PLP}($\leq\approx$ 225 cm^{-1}) are much lower than the ω_{TO} phonon frequency while ω^{+}_{PLP} mode nearly overlaps with the ω_{LO} phonon. Therefore, we expect a very little change in their reflectivity spectra – especially in the reststrahlen band region and anticipate observing only one deep minima in the IRR spectra at $\omega \approx \omega_{LO} \approx \omega^{+}_{PLP}$. In heavily doped GaN films (cf. Sec. 4.1.2), however, significant changes in the spectral features are predicted (see: Fig. 5 c-d)). The observed modifications in the IRR spectra [52] for thicker and heavily doped samples will be discussed next.

Melentev et al. [52] have recently performed IRR measurements on two thick n-GaN samples (M1, M2) with higher N values and observed strikingly different features in the reststrahlen band region. To comprehend these atypical traits – we have reported in Table 3 our calculated values of ω_P, ω^{+}_{PLP} and ω^{-}_{PLP} modes. One may note that in sample M1, the ω_P (≈664 cm^{-1}) falls between ω_{LO} and ω_{TO} phonon frequencies while in sample M2, ω_P (≈1782 cm^{-1}) has a much higher value than the ω_{LO} phonon. Therefore, in M1 one would expect [52] observing two reflectivity minima one near ω^{-}_{PLP} frequency and the other close to the ω^{+}_{PLP} mode. In heavily doped sample M2, however, the superposition of the reststrahlen band and plasma reflection band occurs at a frequency $\omega \leq \omega_{LO}$. In this situation one expects in the IRR reflectivity spectra [52] perceiving one unusual sharp dip near $\omega \approx \omega^{-}_{PLP} \approx \omega_{TO}$ and another minima at $\omega \approx \omega^{+}_{PLP} \approx \omega_P$. In both samples (M1, M2), the results of reflectance spectra reported in Ref. [52] have corroborated our theoretical predictions (cf. Sec 4.1.2) and supported the values of $\omega^{\pm}_{PLP}$ modes reported in Table 3 (see: Fig. 6 also). In the context of Berreman effect [60] one can also estimate N in doped GaN ultrathin epifilms (cf. Sec. 4.1.4).

4.2.2. The Berreman effect

In Fig. 7 a) and 7 b), we have reported our results of the *s*- and *p*-polarized IRR and IRT spectra, respectively for a 2 μm thick GaN/Sapphire film at different angles of incidence θ_a (0°, 10°, 20°, 25° and 30°). The methodology outlined in Sec. 3.1 is followed using the necessary parameters from Table 2 a-b). While the calculations of R_s and T_s depend only on $\tilde{\varepsilon}(\omega)_{\perp}$ of the epifilm and substrate – the simulations of R_p and T_p require both $\tilde{\varepsilon}(\omega)_{\perp}$ and $\tilde{\varepsilon}(\omega)_{\parallel}$.

For the smallest angle θ_a (= 10°) our results revealed no significant changes when comparison is made with the reflectivity and transmission spectra at near normal incidence ($R_s = R_p$; $T_s = T_p$ for $\theta_a = 0°$) – except

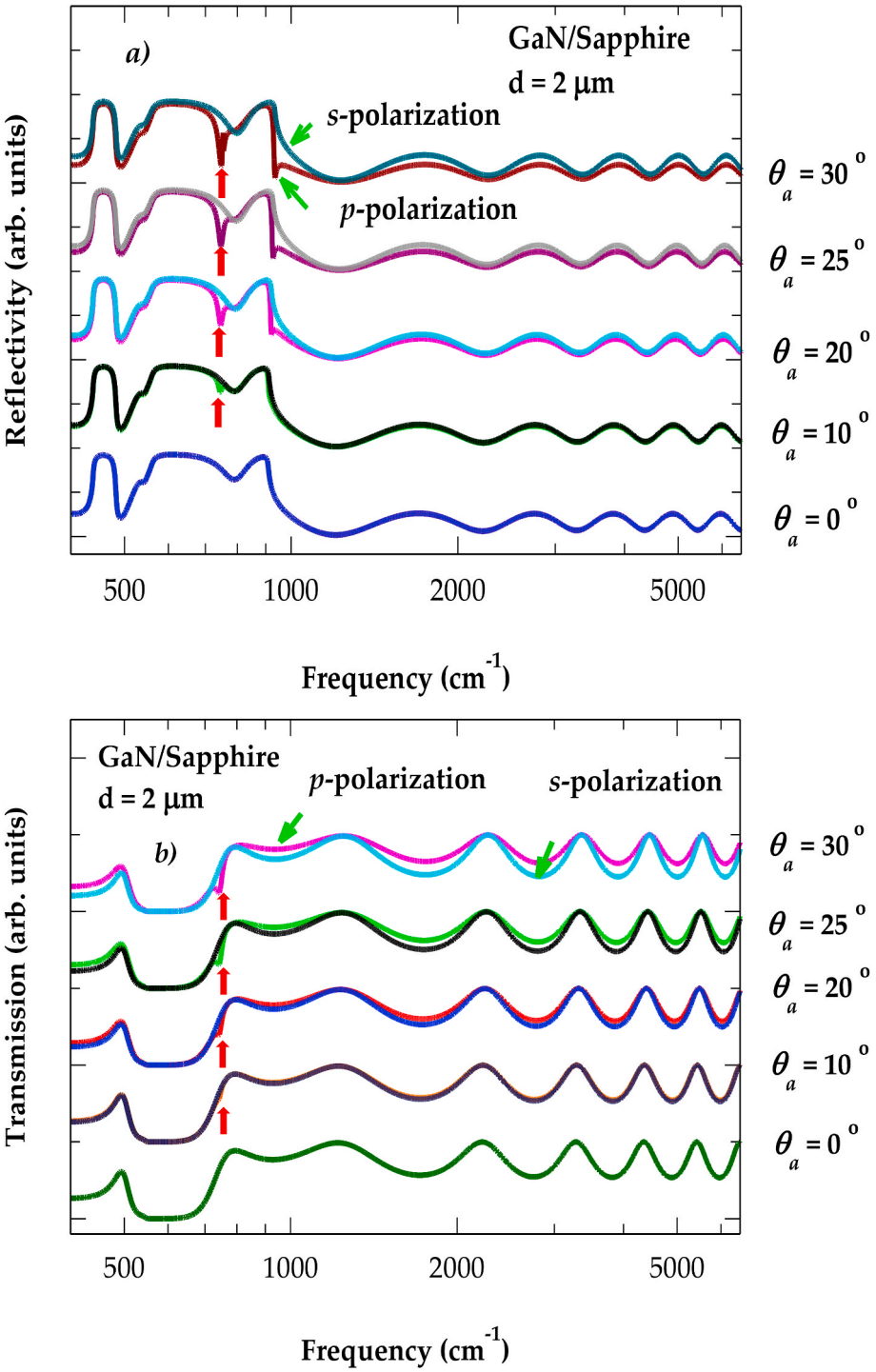

Fig. 7. Simulated results of *s*- and *p*-polarized (a) reflectivity, and (b) transmission spectra on a 2 μm thick GaN film by changing the incident angle of radiation (Berreman effect) from θ_a ($\equiv 0^\circ$, 10°, 20°, 25° and 30°), (c) charge carrier density N dependent simulated *s*- and *p*-polarized reflectivity spectra of a 0.2 μm thick Si-doped GaN/Sapphire at incident angle $\theta_a = 30^\circ$ (see: text).

the observation of a weak dip in R_p and T_p near A_1 (LO) mode. This phonon feature is seen steadily increasing with the increase of angle θ_a where the parallel component of electric field is responsible for exciting the LO mode at non-zero angles. In addition, we have also noticed the E_1 (LO) mode shifting towards the higher frequency side with the decrease of epifilm thickness (not shown) and/or increasing angle θ_a. From these observations it is strongly believed that the Berreman's effect [60] is quite instrumental for identifying the A_1 (LO) phonon and observing the shift of E_1 (LO) mode by changing film thickness d and/or varying angle θ_a.

In Fig. 7 c), we have also displayed our calculations of the IRT spectra at oblique incidence angle, $\theta_a = 30^\circ$ for a thin n-GaN/Sapphire (0.2 μm) epifilm. Clearly, the simulated results in the *p*-polarization exhibited a minimum associated with the TO phonon near ~560 cm^{-1}. This mode is asymmetrically broadened towards the higher energy side – possibly due to the free carrier absorption [52]. The other feature that one can notice

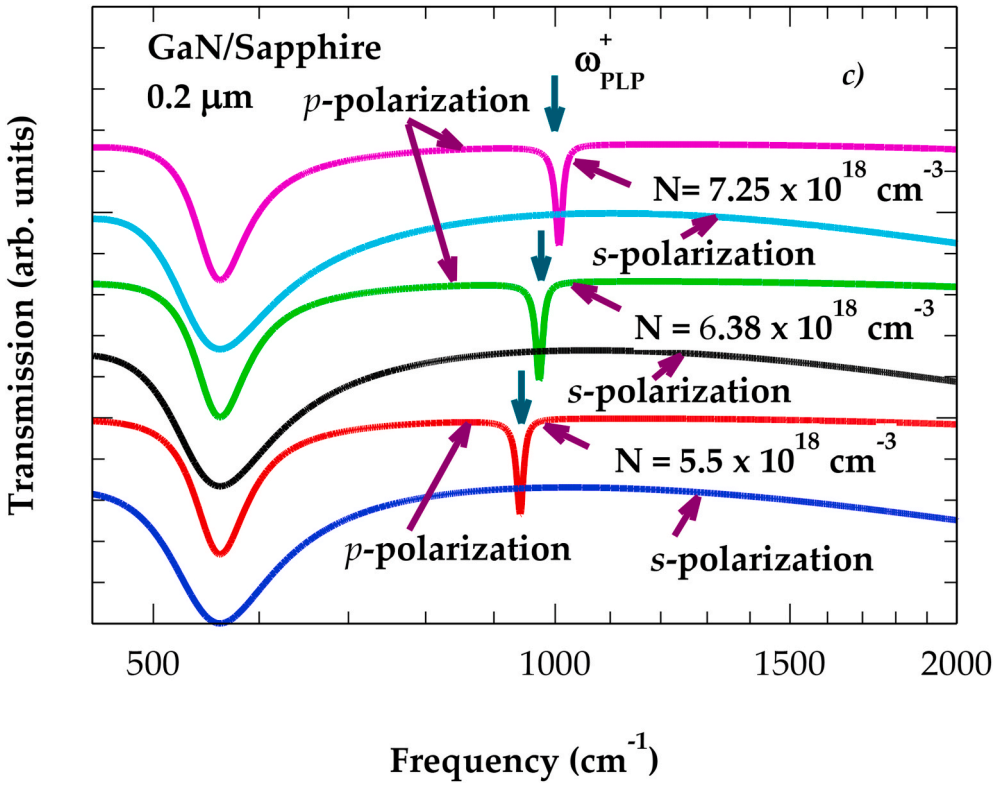

Fig. 7. (*continued*).

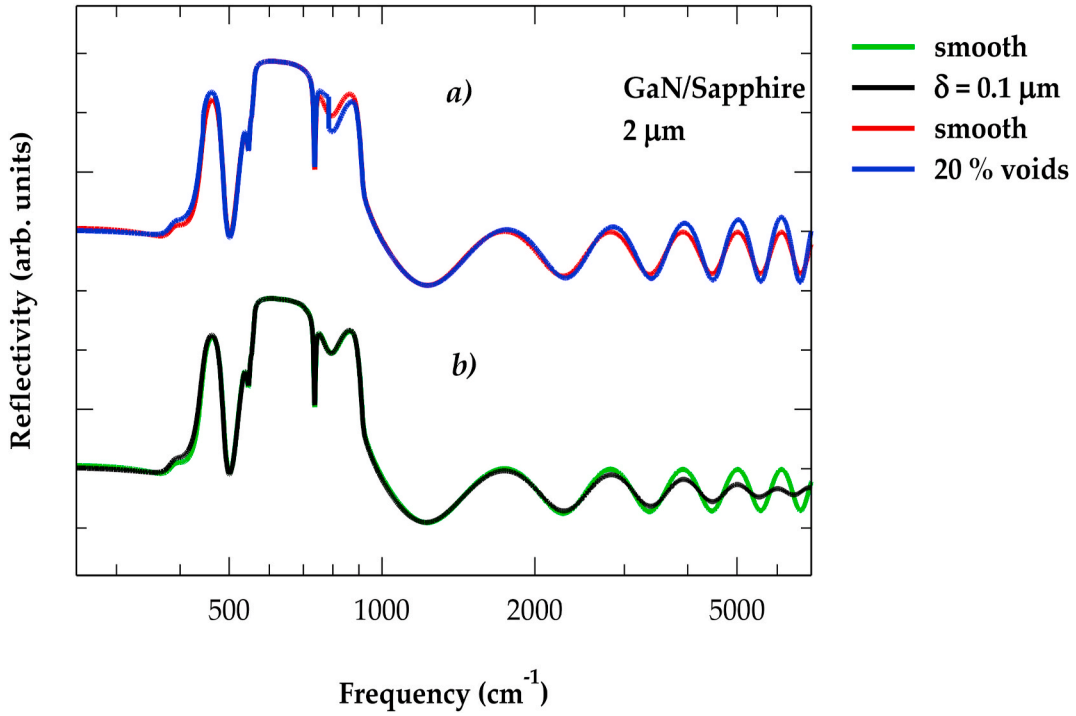

Fig. 8. The effects of surface and interface roughness using Eq. (14) on the simulated reflectivity spectra of a 2 μm thick GaN/Sapphire sample (see: text).

in Fig. 7 c) is a dip (see: bottle green color vertical arrow) which demonstrated a shift towards the higher frequency regime with the increase of free electron concentration, N. As this trait did not emerge in the *s*-polarization we have assigned it to the ω^{+}_{PLP} mode (see: Fig. 7 c)) based on its dependence on N (see Fig. 6) and appearance only in the *p*-polarization. In the context of our earlier assertion on the Berreman effect [60], this revelation of the transmission (T_p) minima (see: Fig. 7 c)) at TO and ω^{+}_{PLP} in the oblique incidence has provided a direct and a simple method of explicating free charge carrier concentration N in thin n-doped GaN epifilms. In our simulations, the projected value of ω^{+}_{PLP} for

Table 4
Best fit optical phonon parameters used in the classical 4 × 4 transfer matrix model for calculating the infrared reflectivity spectra of six different GaN/Sapphire samples. The basic characteristics of each sample are given in Table 1 (see: text).

GaN Sample #	d (μm)	ω_P(cm^{-1})	γ_P (cm^{-1})	$\omega_{TO\parallel}$(cm^{-1})	$\omega_{TO\perp}$ (cm^{-1})	$\omega_{LO\parallel}$ (cm^{-1})	$\omega_{LO\perp}$ (cm^{-1})	γ (cm^{-1})	Δ(μm)
S_0	3.61	50	35	533	561	735	743	5	0.010
S_1	2.47	135	105	533	561	734	743	5	0.016
S_2	1.94	245	200	533	560	734	742	5	0.020
S_3	2	250	150	533	561	735	743	5	0.017
S_4	2.05	380	250	533	560	734	742	5	0.012
S_5	1.67	110	95	533	561	734	743	5	0.014

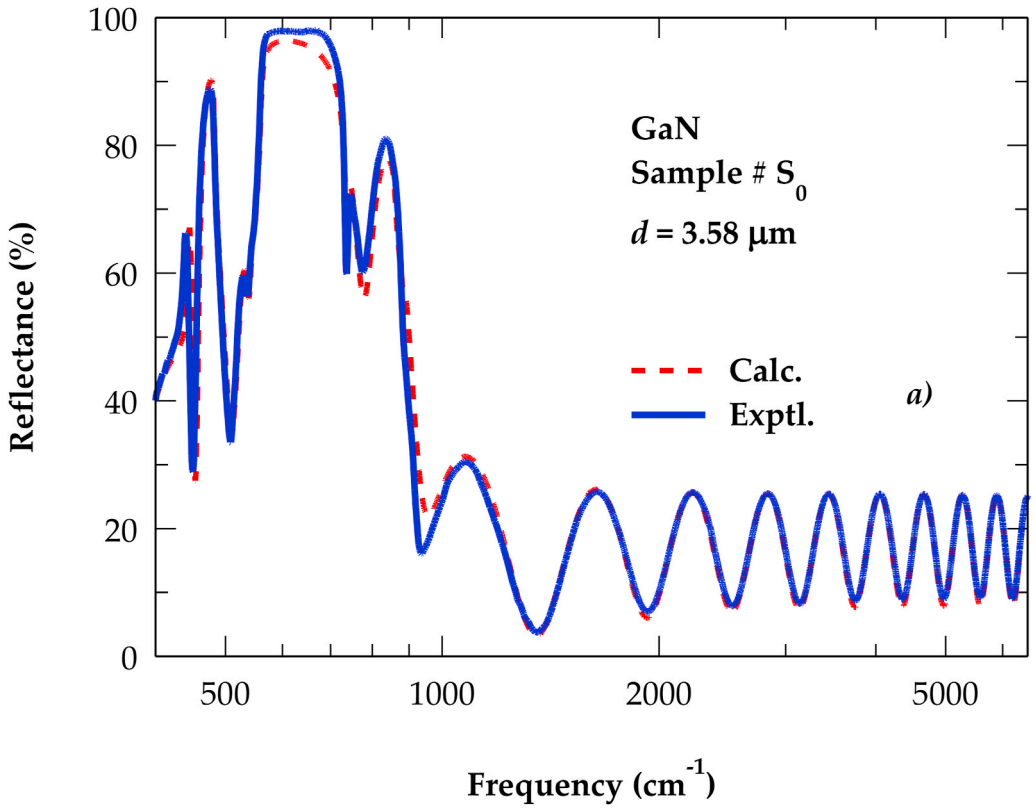

Fig. 9. Comparison of the simulated (red dotted lines) results with the experimental (full blue lines) data of infrared reflectivity spectra (Fig. 9 a - f)) on MOCVD grown GaN/Sapphire samples (#S_0–S_5) using parameter values from Table 4 (see: text). (For interpretation of the references to color in this figure legend, the reader is referred to the Web version of this article.)

different N is in excellent agreement with the IRR [50–52] and RSS [54–56] data. To the best of our knowledge no angular dependent IRT measurements exist at present in the literature for ultrathin Si-doped GaN films. To test this conjecture the only requirement is that the film thickness should be considerably smaller than the reststrahlen wavelength.

4.2.3. Effects of transition layer and surface/interface roughness

The perceptions of ETL and surface roughness in epitaxially grown materials are insinuated in many surface-characterization experiments [37–39] (viz., x-ray photoelectron spectroscopy (XPS), scanning tunneling microscopy (STM), AFM, TEM and inverse photoelectron spectroscopy (IPS), etc.). While the existence of ETL is proposed [39] in GaN/GaAs – its presence in n-GaN/Sapphire has also been ascribed to GaN layer with voids.

To comprehend the observed IRR spectra in Si-doped GaN/Sapphire epifilms, we followed Shokhovets et al., [39] in modifying the optical response theory by including surface roughness δ (in μm) at air/n-GaN and δ_2 (in μm) at n-GaN/TL interfaces. The scattering factors ξ, ξ_2 in the observed ripples at the air/n-GaN and n-GaN/TL interfaces are appropriately incorporated in the IRR formalism – depending upon the interfacial roughness conditions by using wavelength λ of the incident photon and assuming Gaussian distributions [39,49]:

$$\xi = exp\left\{-16(\pi\delta/\lambda)^2\right\} \text{ and } \xi_2 = exp\left\{-16(\pi\delta_2/\lambda)^2\right\}, \quad (14)$$

In Fig. 8 a-b), we have reported the effects of both surface roughness at air/GaN interface and ETL on the simulated reflectivity spectra of a 2 μm thick GaN/Sapphire film. It can be noted that if ETL is assumed as a GaN layer with 20% voids, the simulated reflectivity reveals no appreciable changes on or below the reststrahlen band – it causes, however, significant variations in the Fabry-Perot interference fringe contrasts.

4.3. Experimental analysis of GaN/Sapphire epilayers

To empathize the observed IRR spectra of MOCVD grown GaN/Sapphire samples #S_0 (undoped) and #S_1- #S_5 (Si-doped)) we have pursued a nonlinear "Lovenberg-Marquardt" least square fitting algorithm [64]. In the modified optical response theory, the necessary (see: Table 4) model parameters are extracted by minimizing the error

function, Ξ:

$$\Xi^2 = \frac{1}{\aleph}\sum_{i=1}^{\aleph}\left|R_{i,exp} - R_{i,cal}\right|^2, \quad (15)$$

to help simulate the IRR and IRT spectra. The term $\aleph$ in Eq. (15) represents the number of data points and $R_{i,exp}$, $R_{i,cal}$ are the experimental and calculated values, respectively.

In undoped sample (#S_0) excellent agreement is achieved between the experimental and simulated IRR spectra (see: Fig. 9 a)). Successful application of the 3-phase classical model has demonstrated that the interface of air/film and film/substrate in the sample is abrupt. The conformity of IRR spectra in the "reststrahlen" band region is especially compelling where our theoretical results revealed a flat top with ~96%–100% fits with the experimental data – indicating a very good crystalline quality of the undoped film.

The reflectivity spectra displayed in Fig. 9 b) - 9f) using parameter values from Table 4 show our theoretical results for five Si-doped GaN/Sapphire epifilms of different thickness d (1.62 μm ≤ d ≤ 2.43 μm) and N ≤ 1.12×10^{18} cm^{-3} (see: Table 1). As mentioned before (cf. Sec. 4.1.3) the calculated ω_P values in these samples are much smaller than the A_1 (TO) phonon frequency and the ω^{+}_{PLP} modes overlap with the E_1 (LO) phonon (see: Fig. 6). Consequently, our simulated reflectivity spectra (see: Fig. 9 b) – 9f)) for all samples show no unusual shapes or features – especially in the reststrahlen band region. Comparison of the best fit IRR results using parameter values from Table 4 have not only validated the micro-structural changes observed by TEM and AFM studies at the air/n-GaN and n-GaN/TL interfaces but also corroborated the fact that a moderate Si-doping improves [57,58] the optical as well as the structural properties of GaN/Sapphire epifilms.

5. Conclusions

In summary, we have reported results of a comprehensive experimental and theoretical IRR/IRT study to empathize vibrational and structural properties of MOCVD grown Si-doped GaN/Sapphire samples having different thickness d and carrier concentration N. A classical 4 × 4 transfer matrix method is adopted to simulate the frequency dependent dielectric functions by considering the orientation as well as geometry of the material samples [62]. Careful analysis of the IRR/IRT spectra is achieved by including both the surface roughness and ETL – as revealed in the TEM and AFM studies. By comparing experimental and simulated reflectivity results, we have demonstrated achieving a very good fit to the polarization dependent IRR spectra of Si-doped GaN/-Sapphire samples – allowing accurate determination of the film thickness, charge carrier concentration, root-mean squared roughness and many other parameters. In the context of Berreman effect [60] our simulation of IRT spectra in the oblique geometry for ultrathin Si-doped GaN film has provided a direct evidence of identifying optical phonons and high frequency coupled ω^{+}_{PLP} modes. The shift of PLP mode frequency with charge carrier composition, N is found in very good agreement with the IRR [50–52] and visible RSS [54–56] measurements. To the best of our knowledge, at present no angular dependent IRT measurements exist in the literature for ultrathin Si-doped GaN/-Sapphire films. We hope that our results will encourage spectroscopists to consider using IRT in the oblique geometry as a complementary tool to RSS for characterizing doped III-Ns and/or any ultrathin compound semiconductor films of technological importance. To test our theoretical conjecture the only requirement is that the film thickness should be considerably smaller than the reststrahlen wavelength. In heavily Si-doped GaN, more theoretical work is needed about the anharmonicity especially its role in the coupling mechanism of the PLP ($\omega^{\pm}_{PLP}$) modes with optical lattice phonons. In conclusion, the work presented here has offered valuable information on the surface morphology and phonon features of technologically important Si-doped GaN/Sapphire epifilms. We feel that the knowledge of such material characteristics for n-GaN films is essential for the scientists to evaluate their potential use in designing and/or engineering electronic devices of various industrial applications.

Declaration of competing interest

The authors declare that they have no known competing financial interests or personal relationships that could have appeared to influence the work reported in this paper.

CRediT authorship contribution statement

Devki N. Talwar: Conceptualization, Methodology, Investigation, Writing - review & editing. **Hao-Hsiung Lin:** Writing - review & editing. **Zhe Chuan Feng:** Supervision.

Acknowledgements

One of us (DNT) is thankful to Dr. Deanne Snavely, the Dean of the College of natural sciences and mathematics (C-NSM) at Indiana University of Pennsylvania (IUP) for the travel support and to the IUP Graduate school for the award of an Innovation grant. We thank Dr. Kun Li for his help in the TEM measurements. HH Lin acknowledges the financial support from the Ministry of Science and Technology, Taiwan, under the contract MOST 108-2221-E-002-013-MY3. The work of ZCF was supported in part by a project from the State Key Laboratory of Luminescence and Applications (No. SKLA-2019-06).

References

[1] Sheng Jiang, Yuefei Cai, Feng Peng, Shuoheng Shen, Xuanming Zhao, Peter Fletcher, Volkan Esendag, Kean-Boon Lee, Tao Wang, Exploring an approach toward the intrinsic limits of GaN electronics, ACS Appl. Mater. Interfaces 12 (2020) 12949–12954.

[2] Antonio J. Santos, Bertrand Lacroix, Eduardo Blanco, Hurand Simon, Víctor J. Gómez, Fabien Paumier, Thierry Girardeau, Diana L. Huffaker, Rafael García, Simultaneous optical and electrical characterization of GaN nanowire arrays by means of vis-IR spectroscopic ellipsometry, J. Phys. Chem. **C** 124 (2020) 1535–1543.

[3] Kohei Ueno, Fudetani Taiga, Atsushi Kobayashi, Hiroshi Fujioka, Optical characteristics of highly conductive n-type GaN prepared by pulsed sputtering deposition, Sci. Rep. 9 (2019) 20242.

[4] P. Yew, S.C. Lee, S.F. Cheah, S.S. Ng, H. Abu Hassan, Infrared reflectance characterization of porous GaN thin films on sapphire substrate using factorized-Rayleigh model, Opt. Mater. 96 (2019) 109320.

[5] Erik Stassen, Minhao Pu, Elizaveta Semenova, Evgeniy Zavarin, Wsevolod Lundin, Kresten Yvind, High-confinement gallium nitride-on-sapphire waveguides for integrated nonlinear photonics, Opt. Lett. 44 (2019) 1064–1067.

[6] D. Li, J. Liu, Y. Wang, A. Wu, R. Ruan, Z. Li, Z. Xu Z, Experimental dataset of nanoporous GaN photoelectrode supported on patterned sapphire substrates for photoelectrochemical water splitting, Data Brief 26 (2019) 104433.

[7] Tetsuzo Ueda, GaN power devices: current status and future challenges, Jpn. J. Appl. Phys. 58 (2019) SC0804.

[8] C. Mounir, I.L. Koslow, T. Wernicke, M. Kneissl, L.Y. Kuritzky, N.L. Adamski, S. H. Oh, C.D. Pynn, S.P. DenBaars, S. Nakamura, J.S. Speck, U.T. Schwarz, Localization of current-induced degradation effects in (InAlGa)N-based UV-B LEDs, J. Appl. Phys. 124 (2018), 084504.

[9] Yasuaki Arakawa, Kohei Ueno, Hideyuki Imabeppu, Atsushi Kobayashi, Jitsuo Ohta, Hiroshi Fujioka, Electrical properties of Si-doped GaN prepared using pulsed sputtering, Appl. Phys. Lett. 110 (2017), 042103.

[10] Y. Arakawa, K. Ueno, A. Kobayashi, J. Ohta, H. Fujioka, High hole mobility p-type GaN with low residual hydrogen concentration prepared by pulsed sputtering, APL Mater 4 (2016), 086103 ibid Electrical properties of Si-doped GaN prepared using pulsed sputtering, Appl. Phys. Lett. 110 (2017) 042103.

[11] Wenliang Wang, Haiyan Wang, Weijia Yang, Yunnong Zhu, Guoqiang Li, A new approach to epitaxially grow high-quality GaN films on Si substrates: the combination of MBE and PLD, Sci. Rep. (2016), https://doi.org/10.1038/srep24448.

[12] Y. Cao, R. Chu, R. Li, M. Chen, R. Chang, B. Hughes, High-voltage vertical GaN Schottky diode enabled by low-carbon metal-organic chemical vapor deposition growth, Appl. Phys. Lett. 108 (2016), 062103.

[13] Z. Hu, K. Nomoto, B. Song, M. Zhu, M. Qi, M. Pan, X. Gao, V. Protasenko, D. Jena, H.G. Xing, Near unity ideality factor and Shockley-Read-Hall lifetime in GaN-on-GaN *p-n* diodes with avalanche breakdown Appl, Phys. Lett. 107 (2015) 243501.

[14] S. Fujita, Wide-bandgap semiconductor materials: for their full bloom, Jpn. J. Appl. Phys. 54 (2015), 030101.

[15] N. Tanaka, K. Hasegawa, K. Yasunishi, N. Murakami, T. Oka, 50 A vertical GaN Schottky barrier diode on a free-standing GaN substrate with blocking voltage of 790 V, Appl. Phys. Express 8 (2015), 071001.

[16] T. Oka, T. Ina, Y. Ueno, T. Ina, K. Hasegawa, Vertical GaN-based trench metal oxide semiconductor field-effect transistors on a free-standing GaN substrate with blocking voltage of 1.6 kV, Appl. Phys. Express 7 (2014), 021002.

[17] K. Ueno, E. Kishikawa, S. Inoue, J. Ohta, H. Fujioka, M. Oshima, H. Fukuyama, Effect of growth stoichiometry on the structural properties of AlN films on thermally nitrided sapphire ($11\bar{2}0$), Phys. Status Solidi RRL 8 (2014) 256, 2014.

[18] E. Nakamura, K. Ueno, J. Ohta, H. Fujioka, M. Oshima, Dramatic reduction in process temperature of InGaN-based light-emitting diodes by pulsed sputtering growth technique, Appl. Phys. Lett. 104 (2014), 051121.

[19] J.W. Shon, J. Ohta, K. Ueno, A. Kobayashi, H. Fujioka, Fabrication of full-color InGaN-based light-emitting diodes on amorphous substrates by pulsed sputtering, Sci. Rep. 4 (2014) 5325.

[20] T. Watanabe, J. Ohta, T. Kondo, M. Ohashi, K. Ueno, A. Kobayashi, H. Fujioka, AlGaN/GaN heterostructure prepared on a Si (110) substrate *via* pulsed sputtering, Appl. Phys. Lett. 104 (2014) 182111.

[21] Hiroshi Amano, H. Amano, N. Sawaki, I. Akasaki, Y. Toyada, Metalorganic vapor phase epitaxial growth of a high quality GaN film using an AlN buffer layer, Appl. Phys. 48 (1986) 353. Nobel Lecture, December 8, 2014.

[22] S. Nakamura, T. Mukai, M. Senoh, Si- and Ge-doped GaN films grown with GaN buffer layers, Jpn. J. Appl. Phys. 31 (1992) 2883. S. Nakamura, T. Mukai, M. Senoh, Candela-class high-brightness InGaN/AlGaN double-heterostructure blue-light-emitting diodes, Appl. Phys. Lett. 64 (1994) 1687.; S. Nakamura, M. Senoh, S. Nagahama, T. Yamada, T. Mukai, Superbright Green InGaN Single-Quantum-Well-Structure Light-Emitting Diodes, Jpn J. Appl. Phys. 34 (1995) L1332.

[23] X. Zhang, P. Kung, A. Saxler, D. Walker, T.C. Wang, M. Razeghi, Growth of $Al_xGa_{1-x}N$:Ge on sapphire and silicon substrates, Appl. Phys. Lett. 67 (1995) 1745.

[24] M.A. Khan, Q. Chen, M.S. Shur, B.T. McDermott, J.A. Higgins, J. Burm, W.J. Shaff, L.F. Eastman, CW operation of short-channel GaN/AlGaN doped channel heterostructure field effect transistors at 10 GHz and 15 GHz, IEEE Electron. Device Lett. 17 (1999) 584.

[25] D.D. Koleske, A.E. Wickenden, R.L. Henry, M.E. Twigg, Influence of MOVPE growth conditions on carbon and silicon concentrations in GaN, J. Cryst. Growth 242 (2002) 55.

[26] P.R. Hagemann, W.J. Schaff, J. Janinski, Z. Lilienthal-Weber, n-type doping of wurtzite GaN with germanium grown with plasma-assisted molecular beam epitaxy, J. Cryst. Growth 267 (2004) 123.

[27] Jun Chen, Wei Yi, Takashi Kimura, Shinya Takashima, Masaharu Edo, Takashi Sekiguchi, Cathodoluminescene study of Mg implanted GaN: the impact of dislocation on Mg diffusion, Appl. Phys. Exp. 12 (2019), 051010 and references cited therein.

[28] Sofiane Belahsene, Noor Alhuda Al Saqri, Dler Jameel, Abdelmadjid Mesli, Anthony Martinez, Jacques De Sanoit, Ougazzaden Abdallah, Jean Paul Salvestrini, Abderrahim Ramdane, Henini Mohamed, Analysis of deep level defects in GaN p-i-n diodes after beta particle irradiation, Electronics 4 (2015) 1090.

[29] Umar Saleem, Muhammad Danang Birowosuto, Songyan Hou, Ange Maurice, Beng Kang Tay, Edwin Hang Tong Teo, Maria Tchernycheva, Noelle Gogneau, Hong Wang, Light emission from localised point defects induced in GaN crystal by a femtosecond-pulsed laser, Opt. Mater. Express 8 (2018) 2703.

[30] I. Gîrgel, A. Šatka, J. Priesol, P.- M Coulon, E.D. Le Boulbar, T. Batten, D.W. E. Allsopp, P.A. Shields, Optical characterization of magnesium incorporation in p-GaN layers for core–shell nanorod light-emitting diodes, J. Phys. D Appl. Phys. 51 (2018) 155103.

[31] P.N.M. Ngoepe, W.E. Meyer, F.D. Auret, E. Omotoso, M. Diale, DLTS characterization of defects in GaN induced by electron beam exposure Mat, Sci. Semicond. Proc. 64 (2017) 29.

[32] M.A. Reshchikov, A. Usikov, H. Helava, Yu Makarov, V. Prozheeva, I. Makkonen, F. Tuomisto, J.H. Leach, K. Udwary, Evaluation of the concentration of point defects in GaN, Sci. Rep. 7 (2017) 9297.

[33] Ingo Tischer, Matthias Hocker, Benjamin Neuschl, Manfred Madel, Feneberg Martin, Martin Schirra, Manuel Frey, Manuel Knab, Pascal Maier, Thomas Wunderer, A. Robert, R. Leute, Junjun Wang, Ferdinand Scholz, Johannes Biskupek, Jörg Bernhard, Ute Kaiser, Ulrich simon, levin dieterle, heiko groiss, erich müller, dagmar gerthsen and klaus thonke, optical properties of defects in nitride semiconductors, JMR (J. Mol. Recognit.) 30 (2015) 2977.

[34] Or Chun-tat, Optical Characterization of Defects in GaN, Open Dissertation Press, Hongkong, 2001.

[35] S. Hearne, E. Chason, J. Han, J.A. Floro, J. Figiel, J. Hunter, H. Amano, I.S. T. Tsong, Stress evolution during metalorganic chemical vapor deposition of GaN, Appl. Phys. Lett. 74 (1999) 356.

[36] M. Leszczynski, T. Suski, H. Teisseyre, P. Perlin, I. Grzegory, J. Jun, S. Porowski, T. D. Moustakas, Thermal expansion of gallium nitride, J. Appl. Phys. 76 (1994) 4909.

[37] Z. Benzarti, M. Khelifi, I. Halidou, B.E. Jani, Study of surface and interface roughness of GaN-based films using spectral reflectance measurements, J. Electron. Mater. 44 (2015) 3243–3252.

[38] S. Gupta, Synthesis and characterization of silicon-doped polycrystalline GaN films by r.f. sputtering, Bull. Mater. Sci. 38 (2015) 1163–1170.

[39] S. Shokhovets, R. Goldhahn, V. Cimalla, T.S. Cheng, C.T. Foxon, Reflectivity study of hexagonal GaN films grown on GaAs: surface roughness, interface layer, and refractive index, J. Appl. Phys. 84 (1998) 1561. S. Shokhovets, R. Goldhahn, G. Gobsch, S. Piekh, R. Lantier, A. Rizzi, V. Labedev and W. Richter, Determination of the anisotropic dielectric function for wurtzite AlN and GaN by spectroscopic ellipsometry, J. Appl. Phys. **94** (2003) 307.

[40] M. Hilse, M. Ramsteiner, S. Breuer, L. Geelhaar, H. Riechert, Incorporation of the dopants Si and Be into GaAs nanowires, Appl. Phys. Lett. 96 (2010) 193104.

[41] H. Hijazi, G. Monier, E. Gil, A. Trassoudaine, C. Bougerol, C. Leroux, D. Castellucci, C. Robert-Goumet, P.E. Hoggan, Y. André, N. Isik Goktas, R.R. LaPierre, V. G. Dubrovskii, Si doping of vapor-liquid-solid GaAs nanowires: n-type or p-type? Nano Lett. **19** (2019) 4498–4504.

[42] C. Tessarek, M. Heilmann, E. Butzen, A. Haab, H. Hardtdegen, C. Dieker, E. Spiecker, S. Christiansen, The role of Si during the growth of GaN micro- and nanorods, Cryst. Growth 14 (2014) 1486–1492.

[43] F. Liang, D. Zhao, D. Jiang, Z. Liu, J. Zhu, P. Chen, J. Yang, S. Liu, Y. Xing, L. Zhang, Role of Si and C impurities in yellow and blue luminescence of unintentionally and Si-doped GaN, Nanomaterials 8 (2018) 1026.

[44] T.Y. Lin, W.S. Su, W.S. Su, Y.F. Chen, Investigation of surface properties of Si-doped GaN films by electric force microscopy and photoluminescence, Solid State Commun. 130 (2004) 49.

[45] J. Ibáñez, 1 S. Hernández, E. Alarcón-Lladó, R. Cuscó, L. Artús, S.V. Novikov, C. T. Foxon, E. Calleja, Far-infrared transmission in GaN, AlN, and AlGaN thin films grown by molecular beam epitaxy, J. Appl. Phys. 104 (2008), 033544.

[46] P. Kühne, C.M. Herzinger, M. Schubert, J.A. Woollam, T. Hofmann, An integrated mid-infrared, far-infrared, and terahertz optical Hall effect instrument, Rev. Sci. Instrum. 85 (2014), 071301.

[47] Bogdan I. Tsykaniuk, Andrii S. Nikolenko, Viktor V. Strelchuk, Viktor M. Naseka, Yuriy I. Mazur, Morgan E. Ware, Eric A. DeCuir Jr., Bogdan Sadovyi, Jan L. Weyher, Rafal Jakiela, Gregory J. Salamo, Alexander E. Belyaev, Infrared reflectance analysis of epitaxial n-type doped GaN layers grown on sapphire, Nanoscale Res Lett 12 (2017) 397.

[48] R.T. Holm, P.H. Klein, P.E.R. Nordquist, Infrared reflectance evaluation of chemically vapor deposited β-SiC films grown on Si substrates, J. Appl. Phys. 60 (1986) 1479.

[49] N. Devki, Talwar, zhe chuan feng, chee wee liu and chin-che tin, influence of surface roughness and interfacial layer on the infrared spectra of V-CVD grown 3C-SiC/Si (1 0 0) epilayers, Semicond. Sci. Technol. 27 (2012) 115019.

[50] Z.F. Li, W. Lu, H.J. Ye, Z.H. Chen, X.Z. Yuan, H.F. Dou, S.C. Shen, G. Li, S. J, Chua Carrier concentration and mobility in GaN epilayers on sapphire substrate studied by infrared reflection spectroscopy, J. Appl. Phys. 86 (1999) 2691–2695.

[51] N. Kuroda, T. Kitayama, Y. Nishi, K. Saiki, H. Yokoi, J. Watanabe, M. Cho, T. Egawa, H. Ishikawa, Infrared study on graded lattice quality in thin GaN crystals grown on sapphire, Jpn. J. Appl. Phys. 45 (2006) 646.

[52] G.A. Melentev, D Yu Yaichnikov, V.A. Shalygin, M Ya Vinnichenko, L.E. Vorobjev, D.A. Firsov, L. Riuttanen, S. Suihkonen, Plasmon phonon modes and optical resonances in *n*-GaN, J. Phys.: Conf. Series 690 (2016), 012005.

[53] P. Wisniewski, W. Knapp, J.P. Malzac, J. Camassel, M.D. Bremser, R.F. Davis, T. Suski, Investigation of optically active E_1 transversal optic phonon modes in $Al_xGa_{1-x}N$ layers deposited on 6H–SiC substrates using infrared reflectance, Appl. Phys. Lett. 73 (1998) 1760.

[54] T. Kozawa, T. Kachi, H. Kano, Y. Taga, M. Hashimoto, N. Koide, K. Manabe, Raman scattering from LO phonon-plasmon coupled modes in gallium nitride, J. Appl. Phys. 75 (1994) 1098.

[55] P. Perlin, J. Camassel, W. Knap, T. Taliercio, J.C. Chervin, T. Suski, I. Grzegory, S. Porowski, Investigation of longitudinal-optical phonon-plasmon coupled modes in highly conducting bulk GaN, Appl. Phys. Lett. 67 (1995) 2524.

[56] Hiroshi Harima, Properties of GaN and related compounds studied by means of Raman scattering, J. Phys. Condens. Matter 14 (2002) R967–R993.

[57] W.S. Li, Z.X. Shen, Z.C. Feng, S. Chua, Temperature dependence of Raman scattering in hexagonal gallium nitride films, J. Appl. Phys. 87 (2000) 3332. Z. C. Feng, Raman scattering study on anisotropic property of wurtzite GaN, Opt. Eng. **41** (2000) 2022.

[58] Y.L. Wu, Z.C. Feng, J.-F. Lee, W. Tong, B.K. Wagner, I. Ferguson, Weijie Lu, X-ray absorption and Raman study of GaN films grown on different substrates by different techniques, Thin Solid Films 518 (2010) 7475–7479.

[59] M. Katsikini, F. Pinakidoua, J. Arvanitidis, E.C. Paloura, S. Ves, Ph Komninou, Z. Bougrioua, E. Iliopoulos, T.D. Moustakas, Comparison of Fe and Si doping of GaN: an EXAFS and Raman study, Mater. Sci. Eng. B 176 (2011) 723–726.

[60] D.W. Berreman, Infrared absorption at longitudinal optic frequency in cubic crystal films, Phys. Rev. 130 (1963) 2193.

[61] N. Devki, Talwar, Direct evidence of LO phonon-plasmon coupled modes in n-GaN, Appl. Phys. Lett. 97 (2010), 051902.

[62] M. Schubert, T. Hofmann, C.M. Herzinger, Generalized far-infrared magneto-optic ellipsometry for semiconductor layer structures: determination of free-carrier effective-mass, mobility, and concentration parameters in n-type GaAs, J. Opt. Soc. Am. A20 (2003) 347. A. Kasic, M. Schubert, S. Einfeldt, D. Hommel, and T. E. Tiwald, Free-carrier and phonon properties of *n*- and *p*-type hexagonal GaN films measured by infrared ellipsometry, Phys. Rev. B **62** (2000) 7365.; A. Kasic, Disorder-activated infrared modes and surface depletion layer in highly Si-doped hexagonal GaN, J. Appl. Phys. **89** (2001) 3720.

[63] T.E. Tiwald, J.A. Woollam, S. Zollner, J. Christiansen, R.B. Gregory, T. Wetteroth, S.R. Wilson, A.R. Powell, Carrier concentration and lattice absorption in bulk and epitaxial silicon carbide determined using infrared ellipsometry, Phys. Rev. **B** 60 (1999), 11 464.

[64] K. Levenberg, A method for the solution of certain non-linear problems in least squares, Q. Appl. Math. 2 (1944) 164–168, https://doi.org/10.1090/qam/10666. D. Marquardt, An Algorithm for Least-Squares Estimation of Nonlinear Parameters, SIAM J. Appl. Math. 11 (1963) 431-441 doi:10.1137/0111030.